





Cryo-EM structure of the polyphosphate polymerase VTC reveals coupling of polymer synthesis to membrane transit

Wei Liu^{1,†}, Jiening Wang^{2,†}, Véronique Comte-Miserez³, Mengyu Zhang¹, Xuejing Yu², Qingfeng Chen⁴, Henning Jacob Jessen^{5,6} , Andreas Mayer^{3,*} , Shan Wu^{2,**}  & Sheng Ye^{1,7,***} 

Abstract

The eukaryotic vacuolar transporter chaperone (VTC) complex acts as a polyphosphate (polyP) polymerase that synthesizes polyP from adenosine triphosphate (ATP) and translocates polyP across the vacuolar membrane to maintain an intracellular phosphate (P_i) homeostasis. To discover how the VTC complex performs its function, we determined a cryo-electron microscopy structure of an endogenous VTC complex (Vtc4/Vtc3/Vtc1) purified from *Saccharomyces cerevisiae* at 3.1 Å resolution. The structure reveals a heteropentameric architecture of one Vtc4, one Vtc3, and three Vtc1 subunits. The transmembrane region forms a polyP-selective channel, likely adopting a resting state conformation, in which a latch-like, horizontal helix of Vtc4 limits the entrance. The catalytic Vtc4 central domain is located on top of the pseudo-symmetric polyP channel, creating a strongly electropositive pathway for nascent polyP that can couple synthesis to translocation. The SPX domain of the catalytic Vtc4 subunit positively regulates polyP synthesis by the VTC complex. The noncatalytic Vtc3 regulates VTC through a phosphorylatable loop. Our findings, along with the functional data, allow us to propose a mechanism of polyP channel gating and VTC complex activation.

Keywords coupled polymerase and translocase; cryo-EM; polyP; PP-InsP; VTC

Subject Categories Structural Biology; Membrane & Trafficking

DOI 10.15252/emboj.2022113320 | Received 17 December 2022 | Revised 18

March 2023 | Accepted 27 March 2023 | Published online 17 April 2023

The EMBO Journal (2023) 42: e113320

Introduction

Phosphate (P_i) homeostasis is a tightly regulated process in all organisms. Cells face major changes in demand and supply of P_i, for example, during the S-phase, when DNA is duplicated. While cells must meet these P_i demands, at the same time, they must safeguard themselves against an excessive cytoplasmic P_i concentration, which might have detrimental bioenergetic effects (Austin & Mayer, 2020). How cells maintain an intracellular P_i homeostasis is a fundamental question and of growing interest for medicine and agriculture. Dysfunction of P_i homeostasis leads to neurodegeneration of renal Fanconi syndrome in humans (Legati *et al*, 2015; Ansermet *et al*, 2017), severe growth retardation and dwarfism in plants (Puga *et al*, 2014; Liu *et al*, 2015), and lethality in microorganisms (Sethuraman *et al*, 2001).

To achieve a delicate balance between the biosynthetic requirements for P_i and the risks of excessive cytoplasmic P_i, unicellular organisms maintain important P_i stores in membrane-bound, acidocalcisome-like organelles in the form of inorganic polyphosphates, a polymer of up to a thousand P_i units linked through phosphoric anhydride bonds (Docampo & Huang, 2016). PolyP influences numerous processes in eukaryotes, ranging from activation of inflammatory responses, wound healing and blood clotting (Moreno-Sanchez *et al*, 2012; Hoac *et al*, 2013; Holmstrom *et al*, 2013; Smith & Morrissey, 2014; Hassanian *et al*, 2015; Gerasimaite & Mayer, 2016; Mailer *et al*, 2019; Schepler *et al*, 2022) to the regulation of bone calcification, cation acquisition (Klomp maker *et al*, 2017), protein polyphosphorylation (Azevedo *et al*, 2015, 2018; Bentley-DeSousa *et al*, 2018; Bondy-Chorney *et al*, 2020), protein folding (Gray *et al*, 2014), osmoregulation (Rohloff &

1 Frontiers Science Center for Synthetic Biology (Ministry of Education), Tianjin Key Laboratory of Function and Application of Biological Macromolecular Structures, School of Life Sciences, Tianjin University, Tianjin, China

2 State Key Laboratory of Biocatalysis and Enzyme Engineering, Hubei Collaborative Innovation Center for Green Transformation of Bio-Resources, Hubei Key Laboratory of Industrial Biotechnology, School of Life Sciences, Hubei University, Wuhan, China

3 Département d'Immunobiologie, Université de Lausanne, Epalinges, Switzerland

4 School of Life Sciences, Yunnan University, Kunming, China

5 Institute of Organic Chemistry, University of Freiburg, Freiburg, Germany

6 CIBSS – Centre for Integrative Biological Signalling Studies, University of Freiburg, Freiburg, Germany

7 Life Sciences Institute, Zhejiang University, Hangzhou, China

*Corresponding author. Tel: +86 22 2789 3635; E-mail: andreas.mayer@unil.ch

**Corresponding author. Tel: +86 135 2062 5153; E-mail: wushan91@hubu.edu.cn

***Corresponding author. Tel: +41 21 692 5704; E-mail: sye@tju.edu.cn

†These authors contributed equally to this work

Docampo, 2008; Lander *et al*, 2013), and virulence of a series of pathogens (Ikeh *et al*, 2017). PolyP can also have a major impact on cytosolic P_i homeostasis. Dysregulation of its synthesis can drive cells into P_i starvation or a state of P_i excess (Desfougeres *et al*, 2016). In case of sudden P_i starvation, polyP from acidocalcisome-like vacuoles can guarantee sufficient P_i reserves to finish the next cell cycle and make an ordered transition into a robust quiescent state. PolyP also buffers transient spikes in P_i consumption, which can occur during S-phase (Bru *et al*, 2016b).

In prokaryotes, the polyphosphate kinase PPK1/2 catalyzes the transfer of the γ -phosphate from ATP to produce polyP chains (Akiyama *et al*, 1992). Despite the widespread presence of polyP and acidocalcisome-like vacuoles in eukaryotes, only a single eukaryotic-type polyP-synthesizing enzyme could so far be isolated. This vacuolar transporter chaperone (VTC) complex, originally identified in yeast but with homologs in a wide variety of lower eukaryotes, has provided insights into the mechanisms underlying the polyP synthesis (Hothorn *et al*, 2009). The aim of this study was to address three fundamental questions related to the VTC complex. The first question is related to the stoichiometry and the assembly of native VTC complexes. VTC complexes of *Saccharomyces cerevisiae* contain at least four subunits: Vtc1, Vtc2, Vtc3, and Vtc4 (Cohen *et al*, 1999; Muller *et al*, 2002), for which homologs can readily be identified in other organisms. Vtc1 is a small membrane protein only containing three transmembrane helices. Vtc2, Vtc3, and Vtc4 are highly homologous in sequence, share a similar transmembrane domain with Vtc1 at the C terminus, and have an N-terminal SPX (Syg1/Pho81/XPR1) domain that plays key role in P_i homeostasis (Wild *et al*, 2016), and a tunnel-shaped, central domain (Hothorn *et al*, 2009). The central domain of Vtc4 is a polyP polymerase that synthesizes polyphosphate using ATP as a substrate, while that of Vtc2 or Vtc3 is catalytically inactive (Hothorn *et al*, 2009; Wild *et al*, 2016). A further subunit, Vtc5, can associate with VTC. While its domain structure is similar to that of Vtc2, Vtc3 and Vtc4, the Vtc5 sequence is highly diverged. Vtc5 can stimulate VTC but is not essential for its activity, nor for its regulation by 5-InsP₇, suggesting that it is an optional regulatory subunit (Desfougeres *et al*, 2016). Crystal structures of the central domains of Vtc2 and Vtc4, and the SPX domain of Vtc4 had been determined (Hothorn *et al*, 2009). However, these structures provide no information about the stoichiometry and the assembly of VTC complexes. The second question is related to the functional integrity of VTC complexes. The VTC complex is not only a polyP polymerase but also a polyP translocase. To avoid the toxicity of the accumulation of polyP in the cytoplasm, polyP synthesis and the immediate translocation of polyP into the vacuole are coupled (Gerasimaite *et al*, 2014; McCarthy *et al*, 2022). However, how they are coupled remains unclear. The third question is related to the regulation of VTC complexes. When cytosolic P_i concentration is sufficiently high, VTC complexes should synthesize polyP, while with low cytosolic P_i concentration, VTC complexes should be switched off to avoid depletion of P_i from the cytosol. The activity of VTC complexes is regulated through inositol-based signaling molecules, including the highly phosphorylated, diffusible inositol polyphosphates (InsPs) and inositol pyrophosphates (PP-InsPs; Wild *et al*, 2016; Gerasimaite *et al*, 2017).

To address these questions, we performed functional assays and cryo-EM structural analysis on endogenous *S. cerevisiae* VTC

complex. The cryo-EM structure, as well as the detailed functional assay, reveals an unexpected heteropentameric architecture, a coupled polyP polymerase and translocase, a stimulatory SPX domain, and a phosphorylation-dependent regulatory loop. It provides insights into the activation and regulation mechanism of the VTC complex, as well as the polyP channel gating mechanism.

Results

Purified VTC complex synthesizes polyP in an ATP- and inositol polyphosphate-dependent manner

The VTC complex of *S. cerevisiae* contains four subunits: Vtc1, Vtc2, Vtc3, and Vtc4 (Cohen *et al*, 1999; Muller *et al*, 2002). We first performed pull-down assays and confirmed that no interaction exists between Vtc2 and Vtc3, either directly or indirectly (Fig EV1A), confirming the existence of two different VTC complexes, Vtc4/Vtc3/Vtc1 and Vtc4/Vtc2/Vtc1, as also revealed previously (Hothorn *et al*, 2009). Consistently, knockout of VTC1 or VTC4 alone, or of both VTC2 and VTC3, significantly reduced the cellular PolyP content (Fig 1A), indicating that the catalytic subunit Vtc4 is necessary but not sufficient for polyP synthesis *in vivo*. Individual knockout of VTC2 or VTC3, which disrupted the formation of only one of the two VTC complexes, did not significantly reduce the cellular polyP content (Fig 1A). This indicates that Vtc4/Vtc3/Vtc1 and Vtc4/Vtc2/Vtc1 complexes independently synthesize polyP and suggests a compensatory mechanism to boost the activity of one complex when the other one loses function for the maintenance of the intracellular polyP content.

We inserted an affinity tag (His-TEV-Protein A) at the C terminus of either Vtc3 or Vtc2 and individually purified the endogenous Vtc4/Vtc3/Vtc1 and Vtc4/Vtc2/Vtc1 complexes (Fig EV1B and C). We performed the polyP synthesis experiments on these intact VTC complexes and observed that both Vtc4/Vtc3/Vtc1 and Vtc4/Vtc2/Vtc1 complexes retain the ability to synthesize polyP from ATP *in vitro* in a divalent cation-dependent manner (Fig EV1D and E), in agreement with a previous study revealing that the central domain (Vtc4¹⁸⁹⁻⁴⁸⁰) of Vtc4 is a polyP polymerase (Hothorn *et al*, 2009). The synthesized polyP could be degraded by Ppx1, a polyphosphatase in yeast that specifically hydrolyzes polyP (Fig EV1D). While ATP, GTP, and CTP all interact with the central domain of Vtc4 with binding affinities in the micromolar range (Hothorn *et al*, 2009), polyP synthesis was significantly reduced when ATP was replaced with GTP, an ATP analog sharing a similar purine moiety, and it was completely eliminated upon the replacement of ATP with CTP (Fig 1B and C). These data demonstrate that polyP synthesis by the VTC complex is preferentially driven by ATP.

We next measured polyP synthesis as a function of ATP concentration (Fig 1D). VTC activity showed a steep, linear dependence on ATP concentration, reaching saturation at 3–4 mM. With a K_m value of around 2 mM ATP, VTC shows a low affinity for ATP, which could be relevant to regulate VTC activity in the cellular context, as free cellular ATP levels in yeast have been estimated to be ~1–2 mM (Ingram & Barnes, 2000; Ozalp *et al*, 2010; Pluskal *et al*, 2011). In a situation where P_i is abundant and VTC is maximally activated through inositol pyrophosphates (PP-InsPs), the high K_m value for ATP provides an inbuilt mechanism to downregulate polyP

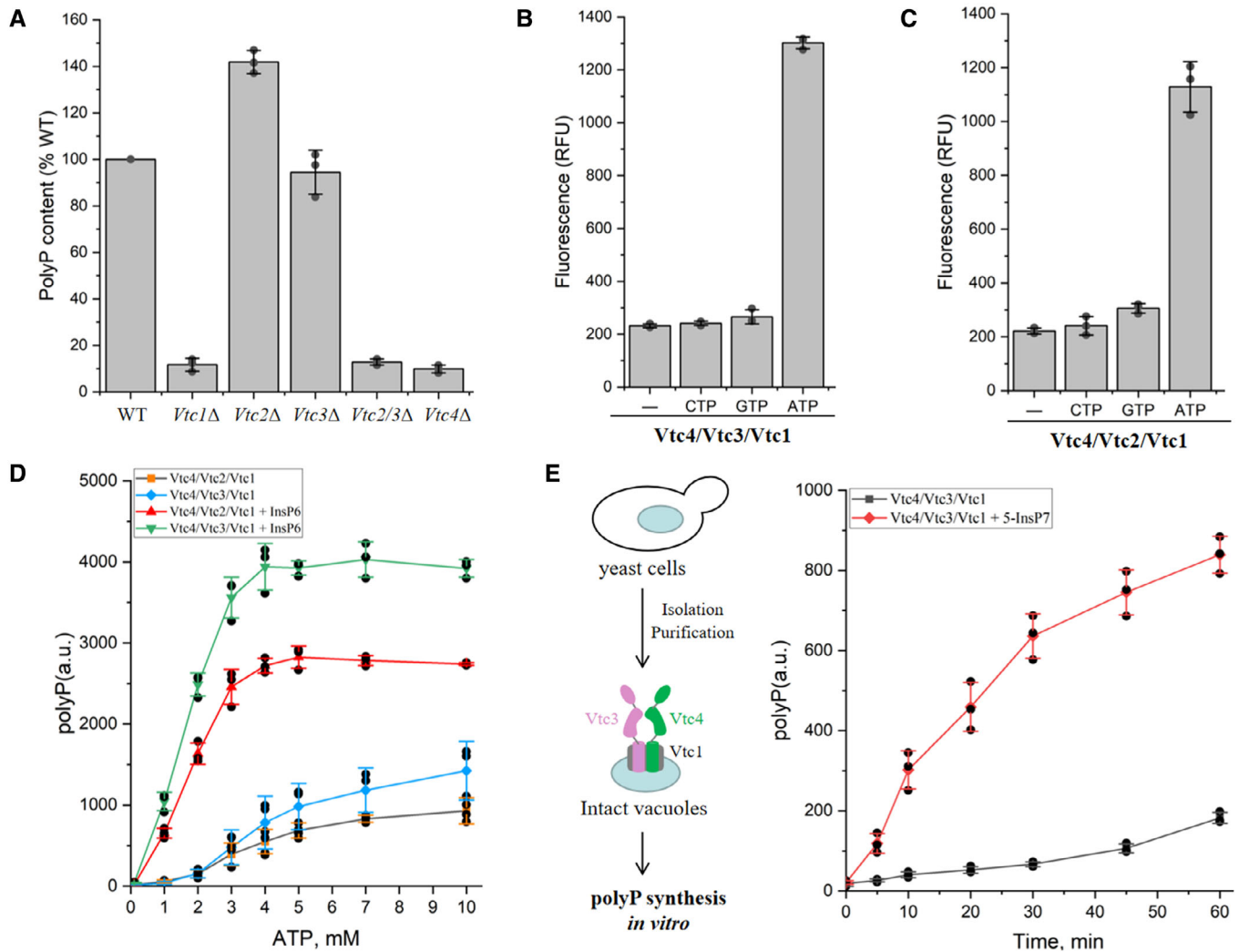


Figure 1. Functional characterization of VTC complexes.

- A PolyP accumulation *in vivo*. The polyP content of wild-type cells was set to 100%. Knockout of *Vtc1*, *Vtc2*, *Vtc3*, or *Vtc4* impacts cellular polyP levels. Data show the mean \pm s.d. (biological replicates $n = 3$).
- B, C Purified endogenous (B) *Vtc4/Vtc3/Vtc1* and (C) *Vtc4/Vtc2/Vtc1* complexes synthesize polyP from ATP, GTP or CTP *in vitro*. 6 μ g of *Vtc4/Vtc3/Vtc1* complex or *Vtc4/Vtc2/Vtc1* complex and 5 mM ATP/GTP/CTP were incubated for 60 min at 4°C, the reaction was stopped by the addition of 15 mM EDTA and 15 μ M DAPI, and fluorescence was measured. Data show the mean \pm s.d. (biological replicates $n = 3$).
- D PolyP synthesis curves of purified endogenous *Vtc4/Vtc3/Vtc1* and *Vtc4/Vtc2/Vtc1* complexes at different ATP concentrations in the absence or presence of 10 mM InsP₆ *in vitro*. The reaction system is detailed in [Materials and Methods](#). Data show the mean \pm s.d. (biological replicates $n = 3$).
- E PolyP synthesis by isolated vacuoles carrying VTC complexes in the absence or presence of 1 μ M 5-InsP₇ *in vitro*. The reaction system is detailed in [Materials and Methods](#). Data show the mean \pm s.d. (biological replicates $n = 3$).

Source data are available online for this figure.

synthesis if ATP supply of the cell runs low, avoiding depletion of the essential ATP pool for building phosphate reserves. In this way, VTC could integrate cellular energy status with the InsPP and SPX-dependent signaling of P_i availability through the intracellular phosphate reception and signaling pathway (Austin & Mayer, 2020).

In response to cellular P_i availability, PP-InsPs stimulate polyP synthesis. In line with this, InsPs and PP-InsPs can activate VTC *in vitro* (Lonetti et al, 2011; Wild et al, 2016; Gerasimaite et al, 2017). While inositol pyrophosphates activate VTC more strongly and at lower concentrations than InsP₆ (Gerasimaite et al, 2017), InsP₆ is

commercially available and was used for many of our *in vitro* experiments for that reason. We simplified the strain background because the two VTC complexes are enzymatically redundant. Analyzing the effect of substitutions would hence necessitate to genetically manipulate both complexes in parallel. Furthermore, only the *Vtc3*-containing complex resides entirely on vacuoles, whereas much of the *Vtc4/Vtc2/Vtc1* resides in the cell periphery (probably in the ER; Uttenweiler et al, 2007). To streamline the approach, we focused the analysis on substitutions in the *Vtc4/Vtc3/Vtc1* complex and performed all further analyses

in *VTC2* knockout cells to exclude interference by the Vtc4/Vtc2/Vtc1 complex.

PolyP synthesis by purified Vtc4/Vtc3/Vtc1 complex was strongly stimulated by InsP_6 , especially at low concentrations of ATP (Fig 1D). Without the addition of ATP, InsP_6 alone did not produce a fluorescence signal (Fig EV1F), demonstrating the regulatory role of InsP_6 . Given that the VTC complex integrated in the intact membrane displays much higher activity than the purified complex (Gerasimaite *et al*, 2014), we also performed *in vitro* polyP synthesis experiments using isolated vacuoles. As shown in Fig 1E, the VTC complex from isolated vacuoles synthesized polyP in an ATP-dependent manner, and PP- InsP_6 enhanced polyP synthesis by more than 10-fold.

Overall architecture of yeast Vtc4/Vtc3/Vtc1 complex

To understand the polyP synthesis and transport mechanism, we analyzed the purified Vtc4/Vtc3/Vtc1 complex by single-particle cryo-electron microscopy (Cryo-EM), yielding a structure at an overall resolution of 3.1 Å (Appendix Figs S1 and S2). The cryo-EM density map was of sufficient quality to allow modeling of almost the entire complex, including the N-terminal SPX domains, the central domains, the C-terminal transmembrane (TM) domains of Vtc4 and Vtc3, and the TM domains of Vtc1 (Fig EV2A).

The structure of the Vtc4/Vtc3/Vtc1 complex reveals an unexpected heteropentameric architecture with a subunit stoichiometry of one Vtc4, one Vtc3, and three Vtc1 subunits (Fig 2A). The transmembrane domains of Vtc1, Vtc3, and Vtc4, which share approximately 15% amino acid sequence identity, adopt similar backbone conformations (Fig 2B). Three transmembrane helices (TM1-TM3) from each subunit assemble in a pseudo-symmetrical fashion forming a cylinder-shaped pentameric transmembrane domain. When viewed from the cytoplasmic side, the arrangement of subunits around the transmembrane domain is Vtc3-Vtc4-Vtc1-Vtc1-Vtc1 in a counter-clockwise direction (Fig 2C). The arrangement results in a different subunit packing environment for each Vtc1. We therefore refer to the three Vtc1 subunits as Vtc1(α), Vtc1(β), and Vtc1(γ) for clarity (Fig 2C). The TM1 helices from each subunit form an inner ring lining a pore, which likely represents the central pore for polyP translocation into the vacuole. The pore tapers as it traverses toward the intravacuolar side of the membrane. The TM2 and TM3 helices from each subunit form an outer ring surrounding the inner ring. Compared with Vtc1 or Vtc4, the TM part of Vtc3 has an additional, amphipathic MX helix at the C terminus (Fig EV2B). The MX helix of Vtc3 runs parallel to the vacuolar face of the membrane, forming hydrophobic interactions with the TM2 and TM3 helices of Vtc4, and the TM3 helix of Vtc3 (Fig EV2C). Given that Vtc2 and Vtc3 share an MX helix with high sequence identity (Appendix Fig S3), the MX helix of Vtc2 likely adopts the same conformation and performs similar function in the Vtc4/Vtc2/Vtc1 complex in comparison with that of Vtc3 in the Vtc4/Vtc3/Vtc1 complex.

The structure of the Vtc4/Vtc3/Vtc1 complex reveals an asymmetrical arrangement of the cytosolic region in contrast to the relatively symmetrical arrangement of the transmembrane region. Vtc4, Vtc3, and Vtc2 all contain an N-terminal SPX domain, a central domain, and a C-terminal transmembrane domain (Hothorn *et al*, 2009; Wild *et al*, 2016). The central domain (Vtc4¹⁸⁹⁻⁴⁸⁰) of

Vtc4 is a polyP polymerase, while those of Vtc2 and Vtc3 are catalytically inactive, likely playing an accessory function (Hothorn *et al*, 2009). Correspondingly, the catalytically active central domain of Vtc4 is the only cytosolic domain that interacts with the transmembrane pore (Fig EV2A). The catalytically inactive central domain of Vtc3 stacks on top of the central domain of Vtc4 in a head-to-tail manner, forming a heterodimer (Fig 2D). Interestingly, the two SPX domains adopt different positions relative to the respective central domains. The SPX domain of Vtc4 locates at one side of the central domain of Vtc4, using its α I and α IV helices to interact with the α 1 and α 6 helices and the β 6 and β 7 strands of the central domain of Vtc4 (Fig 2D). By contrast, the SPX domain of Vtc3 locates at the other side of the central domain of Vtc3, using a different set of α -helices (α I, α IV, α V, α VI, and α VII) to interact with three α -helices (α 2, α 8, and α 9) and two β strands (β 4 and β 5) of the central domain of Vtc3 (Fig 2D). The asymmetrical arrangement of the cytosolic region of the Vtc4/Vtc3/Vtc1 places both SPX domains close to each other on the same side of the complex (Fig 2D). The SPX domain of Vtc4 not only interacts with the central domain of Vtc4 but also interacts with two α -helices (α 1 and α 9) of the central domain of Vtc3 (Fig 2D). By contrast, the SPX domain of Vtc3 only interacts with the central domain of Vtc3 (Fig 2D).

PolyP channel in a resting and fastened state

The transmembrane domain of the Vtc4/Vtc3/Vtc1 complex resembles a cylinder formed from five subunits in a pseudo-symmetrical arrangement about a central axis. The pore is lined by five TM1 helices, forming “rings” of positively charged residues. The cytoplasmic vestibule of the VTC channel contains two positively charged rings, with K24 of Vtc1, K698 of Vtc3, and K622 of Vtc4 forming one, and R31 of Vtc1, R705 of Vtc3, and R629 of Vtc4 forming the other one, rendering the surface strongly electropositive (Fig 3A and B). These positively charged rings may constitute a polyP selectivity filter in the vestibule of the VTC channel and probably serve to attract polyP to the channel mouth. To test the role of these rings for polyP synthesis and translocation, we created 6 charge-reversing point mutations. All these mutations significantly reduced cellular polyP content (Fig EV3A), in line with previous observations (Gerasimaite *et al*, 2014).

The TM1 helices taper inwards from the cytosolic side to the intravacuolar side, with a ring of hydrophobic residues, including M42 of Vtc1, L716 of Vtc3, and L640 of Vtc4, defining the narrowest point, just 4 Å in diameter (Fig 3C–E). Since this point is too narrow to permit the passage of polyP (with a Pauling radius of 3 Å), the structure likely represents a nonconducting resting state of the pore.

In addition, the cytosolic entrance of the PolyP channel is fastened by a latch-like, horizontal helix (HH) (Fig 3F and G). This helix is part of a linker of over hundred residues connecting the central domain and the transmembrane domain of Vtc4 (Appendix Fig S3). The majority of the residues are hydrophilic, without density in the cryo-EM map, indicating that the linker is highly flexible. However, the N-terminal part of the linker (⁵⁰⁸DFEDEDDEDAALVAAMT⁵²⁴), which is rich in acidic residues, forms an α -helix horizontally latching the entrance of the transmembrane channel (Fig 3G). The N terminus of the helix nestles at the Vtc1(γ)-Vtc3 interface, with the acidic residues forming multiple salt bridges with

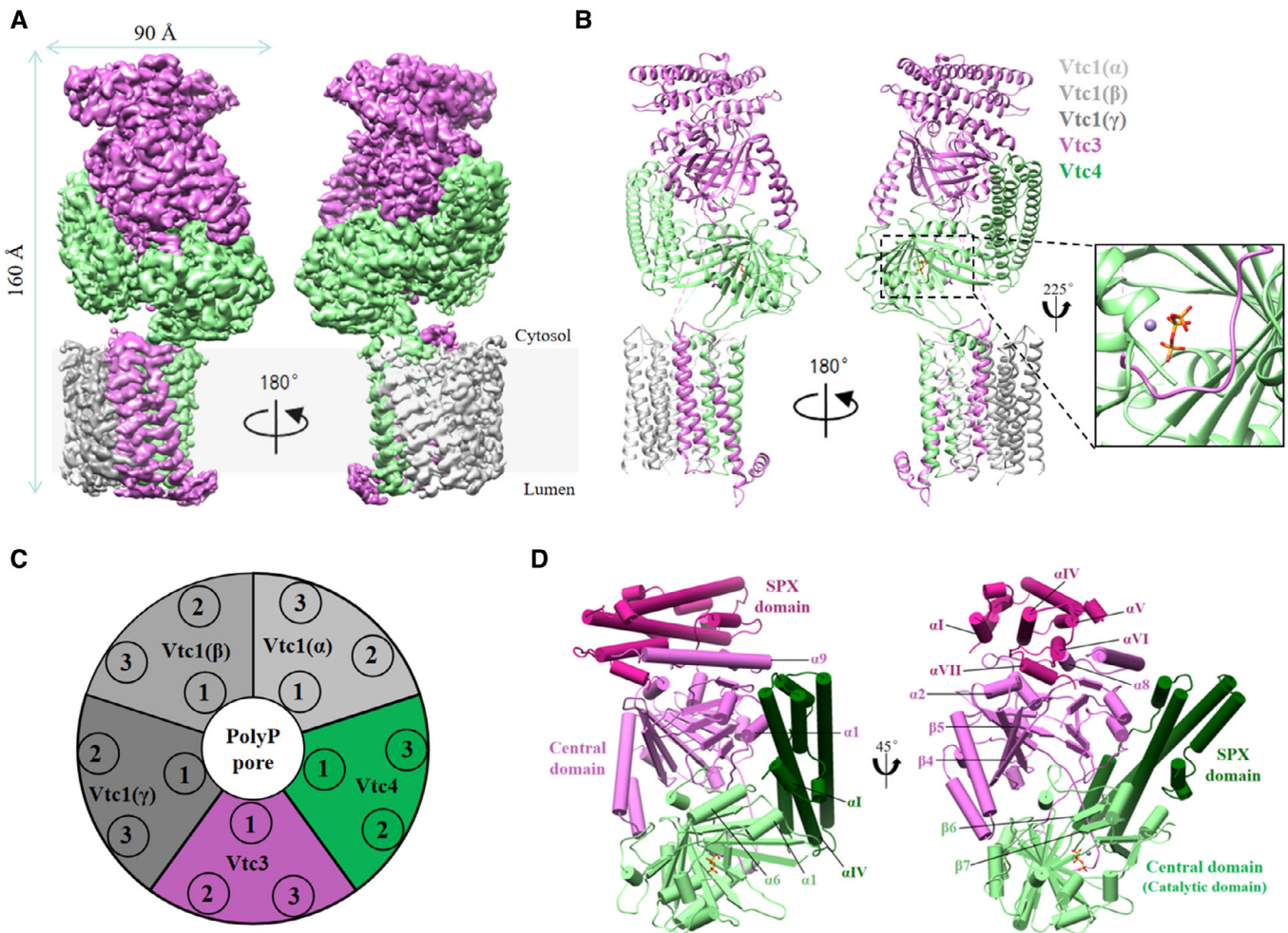


Figure 2. Structure of the yeast Vtc4/Vtc3/Vtc1 complex.

- A Cryo-EM 3D map of the Vtc4/Vtc3/Vtc1 complex, showing front and back views. Color codes for the subunits of the complex are indicated.
- B An atomic model shown in cartoon and colored as in (A). The triphosphate and Mn^{2+} are shown in orange and brown, respectively.
- C Top view of the model of Vtc4/Vtc3/Vtc1 complex. The numbers 1, 2, and 3 represent TM1, TM2 and TM3, respectively, where TM1 is at the N terminus of the sequence and TM3 is at the C terminus of the sequence.
- D Structure of the asymmetrical arrangement of the intracellular region of the Vtc4/Vtc3/Vtc1 complex. The SPX domain and central domain of Vtc3 are shown in violet red and orchid, respectively; the SPX domain and central domain of Vtc4 are shown in dark green and light green, respectively.

the positively charged residues at the channel mouth (Fig 3G). The C terminus of the helix forms multiple hydrophobic interactions with Vtc1(α) and Vtc1(β) (Fig 3G). To probe the importance of this

horizontal helix, we deleted it (residues 508–524) from Vtc4 and observed an approximately 20% higher cellular polyP content in the respective mutant (Fig EV3B).

Figure 3. Conductance and permeation pore structure of the Vtc4/Vtc3/Vtc1 complex.

- A Cutaway of the Vtc4/3/1 complex showing the electrostatic surface potential along the polyP-conducting pathway, excluding the horizontal helix, HH. The transparency of the electrostatic surface potential is set to 0.5.
- B Side and top views of the structure of TM1 of Vtc4/Vtc3/Vtc1 complex. The cytoplasmic vestibule of the VTC channel contains two positively charged rings, with K24 of Vtc1, K698 of Vtc3, and K622 of Vtc4 forming one, and R31 of Vtc1, R705 of Vtc3, and R629 of Vtc4 forming the other one.
- C TM1 α -helices from opposing Vtc1(β) and Vtc3 subunits with side chains shown for pore-lining residues. Spheres represent the solvent-accessible volume of the polyP channel. The black arrow points to the narrowest point of the channel.
- D TM1 α -helices from opposing Vtc1(β) and Vtc4 subunits with side chains shown for pore-lining residues. Spheres represent the solvent-accessible volume of the polyP channel. The black arrow points to the narrowest point of the channel.
- E Profile of the pore radius of the Vtc4/Vtc3/Vtc1 complex.
- F Cutaway of the Vtc4/Vtc3/Vtc1 complex showing the electrostatic surface potential along the polyP-conducting pathway, including the horizontal helix, HH. The transparency of the electrostatic surface potential is set to 0.5.
- G Side and top views of the structure of transmembrane helices of Vtc4/Vtc3/Vtc1 complex. Horizontal helix, HH ($^{\text{F508DFDEDEDDAALVAAMT}^{\text{524}}$).

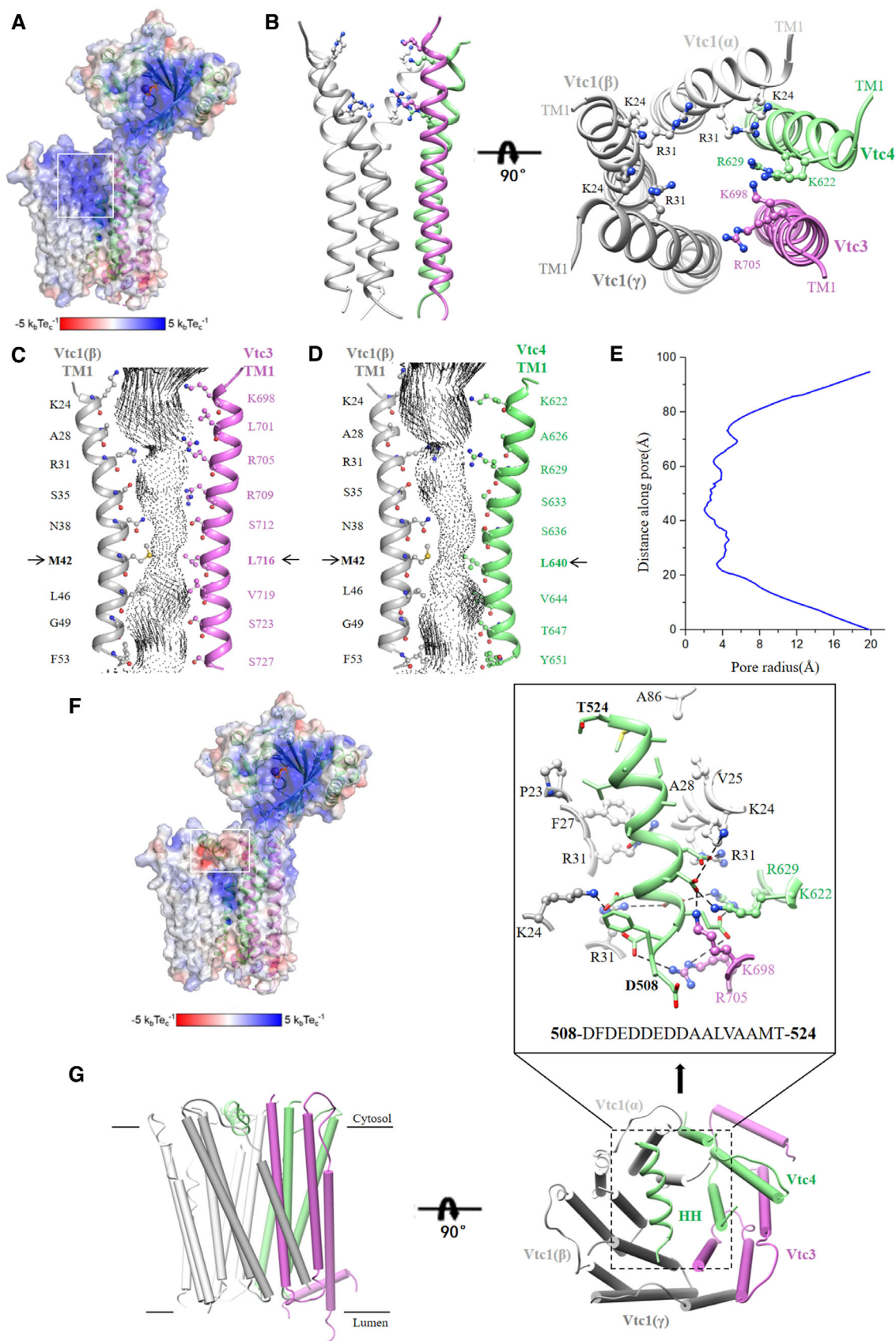


Figure 3.

Coupled polyP synthesis and translocation

The structure of the Vtc4/Vtc3/Vtc1 complex clearly supports the concept of a coupled polyP polymerase and translocase. The structures of the two central domains of the Vtc4/Vtc3/Vtc1 complex are highly similar, with a r.m.s. deviation of 1.8 Å for 276 C α atoms. Both central domains contain a central tunnel formed by antiparallel β strands, with the majority of the α -helices flanking the tunnel wall. The α -helix (α 7) at the C terminus of the central domain of Vtc4 forms a “helical plug” at one end of the tunnel, reducing the tunnel to a small size only allowing polyP to pass (Appendix Fig S4). The central domain of Vtc3 contains two additional α -helices (α 8 and α 9) at the C terminus (Appendix Fig S4). These additional α -helices, together with the SPX domain of Vtc3, completely block one end of the tunnel of the central domain of Vtc3, likely rendering it inactive (Appendix Fig S4). The tunnel walls are lined by conserved basic residues (Fig 4A). Confirming its role as the catalytically active subunit of a polyP polymerase, the Vtc4 central domain shows an endogenous Mn²⁺-bound triphosphate in the tunnel center (Appendix Fig S5). The Mn²⁺ is chelated by carboxylate oxygens of E426 and the triphosphate oxygens in a distorted square-based pyramidal configuration (Fig 4A). The triphosphate is coordinated by six conserved basic residues (K200, R264, R266, K281, R361, and K458), a serine (S457) and a tyrosine (Y359) (Fig 4A). These residues are critical for polyP synthesis, as alanine mutations of K200, R264, R266, K281, R361, K458, S457, and the phenylalanine mutation of Y359, all significantly reduce polyP content of respective mutant cells (Fig 4B). Structure-based sequence alignment revealed that among these residues, the only difference is K458 of Vtc4, which is I522 in Vtc2, and L527 in Vtc3 (Appendix Fig S6A–D). Substituting K458 of Vtc4 to either leucine or isoleucine significantly reduced polyP content, underlining the critical role of K458 for polyP synthesis (Fig 4B).

Although the central domain and the transmembrane domain of Vtc4 are covalently connected, the majority of the linker in between is flexible without observable density in the cryo-EM map. The central domain of Vtc4 interacts with the transmembrane pore via contacts between the β 4- β 5 loop of Vtc4 and the TM2-TM3 loop of Vtc3, as well as contacts between the loop before TM1 of Vtc4 and the β 4- β 5 loop, α 2, and the loop after β 11 of Vtc4 (Fig 4C). The β 4- β 5 loop of Vtc4 is extended and protrudes into a hydrophobic pocket formed between the transmembrane domains of Vtc3 and Vtc4, with the aromatic side chain of Trp287 interacting with Val699, Leu774 and Leu765 of the TM2-TM3 loop of Vtc3, and Pro621 of the loop before TM1 of Vtc4 (Fig 4C). To confirm the importance of the observed interactions between the central domain of Vtc4 and the transmembrane pore, we created point mutants designed to disrupt the hydrophobic contact by changing hydrophobic residues to acidic residues and observed that they all significantly reduce cellular polyP content (Fig 4D).

The interactions bring the catalytically active central domain of Vtc4 in close proximity to the transmembrane pore, with the tunnel walls directly connecting to the vestibule of the pore. Superposition of the previously determined central domain of Vtc4 (Hothorn et al, 2009) with the one determined in this study reveals that the phosphate polymer overlaps with the triphosphate and winds through the tunnel toward the vestibule of the pore (Fig 4E), suggesting that the nascent polyP travels from the active site of the

central domain of Vtc4 to the vestibule of the transmembrane pore, thus translocating across the membrane. In addition, the traveling pathway of polyP is strongly electropositive, which probably feeds the polyP product through the membrane pore into the lumen of the vacuole. To confirm the importance of the electropositive pathway, we created point mutants designed to switch the electrostatic potential by changing positively charged residues to acidic residues and observed that the intracellular content of polyP was significantly reduced (Fig 4F).

The SPX domain of Vtc4 is critical for polyP synthesis and PP-InsPs regulation

Both Vtc3 and Vtc4 contain an N-terminal SPX domain that may relay information about the cellular P_i levels. The structures of the two SPX domains are highly similar, with a r.m.s. deviation of 1.7 Å for 135 C α atoms. Both SPX domains share an N-terminal helical hairpin formed by two small helices, α I and α II, and a three-helix bundle formed by two long helices, α III and α IV, together with two smaller C-terminal helices, α V and α VI (Appendix Fig S3). The SPX domain of Vtc3 contains an additional helix, α VII, at the C terminus (Fig 5A), forming hydrophobic interactions with α IV and α VI helices (Fig 5A). Both SPX domains harbor a positively charged surface formed by multiple conserved lysine residues from helices α II and α IV (Appendix Fig S7B and C) and can interact with a phosphate-containing ligand with little specificity and selectivity (Wild et al, 2016).

An interesting aspect of the Vtc4/Vtc3/Vtc1 complex is that the SPX domain of Vtc4 interacts with both the central domain of Vtc3 and Vtc4 while the SPX domain of Vtc3 only interacts with the central domain of Vtc3. To probe the role of the two SPX domains, we individually truncated the SPX domain of Vtc3 or Vtc4 and performed polyP synthesis experiments on the purified mutant Vtc4/Vtc3/Vtc1 complexes (Appendix Fig S8A and B). Truncation of the SPX domain of Vtc3 reduced polyP synthesis activity of the complex only slightly and preserved the stimulation of its activity by InsP₆ (Fig EV4A), indicating that the SPX domain of Vtc3 is not essential for stimulation of polyP synthesis by InsP₆. By contrast, truncation of the SPX domain of Vtc4 significantly impaired polyP synthesis activity of the Vtc4/Vtc3/Vtc1 complex (Fig EV4A) and addition of InsP₆ reduced this activity further instead of stimulating it (Fig EV4A). Thus, the SPX domain of Vtc4 is critical for polyP synthesis and InsP₆ regulation. Isolated vacuoles carrying the truncated Vtc4/Vtc3/Vtc1 complex lacking the SPX domain of Vtc4 completely lose polyP synthesis activity. Furthermore, addition of 5-InsP₇ or 1,5-InsP₈ no longer stimulates the polyP synthesis activity (Fig 5B). While vacuoles carrying a truncation of the SPX domain of Vtc3 generate less polyP than wild-type, addition of 5-InsP₇ or 1,5-InsP₈ enhances this polyP synthesis activity (Fig 5B). Taken together, the data of purified complex and isolated vacuole all demonstrate that the SPX domain of Vtc4 is critical for polyP synthesis and PP-InsPs regulation.

The structure of the Vtc4/Vtc3/Vtc1 complex reveals that the positively charged surface of the SPX domain of Vtc4 is close to the α 1 helix of Vtc3 (Fig 5C). Two arginine residues of the α 1 helix of Vtc3, R223 and R226, are strictly conserved between Vtc2 and Vtc3 (Appendix Fig S3). To probe the potential role of these conserved arginine residues in InsP₆ regulation, we substituted them with

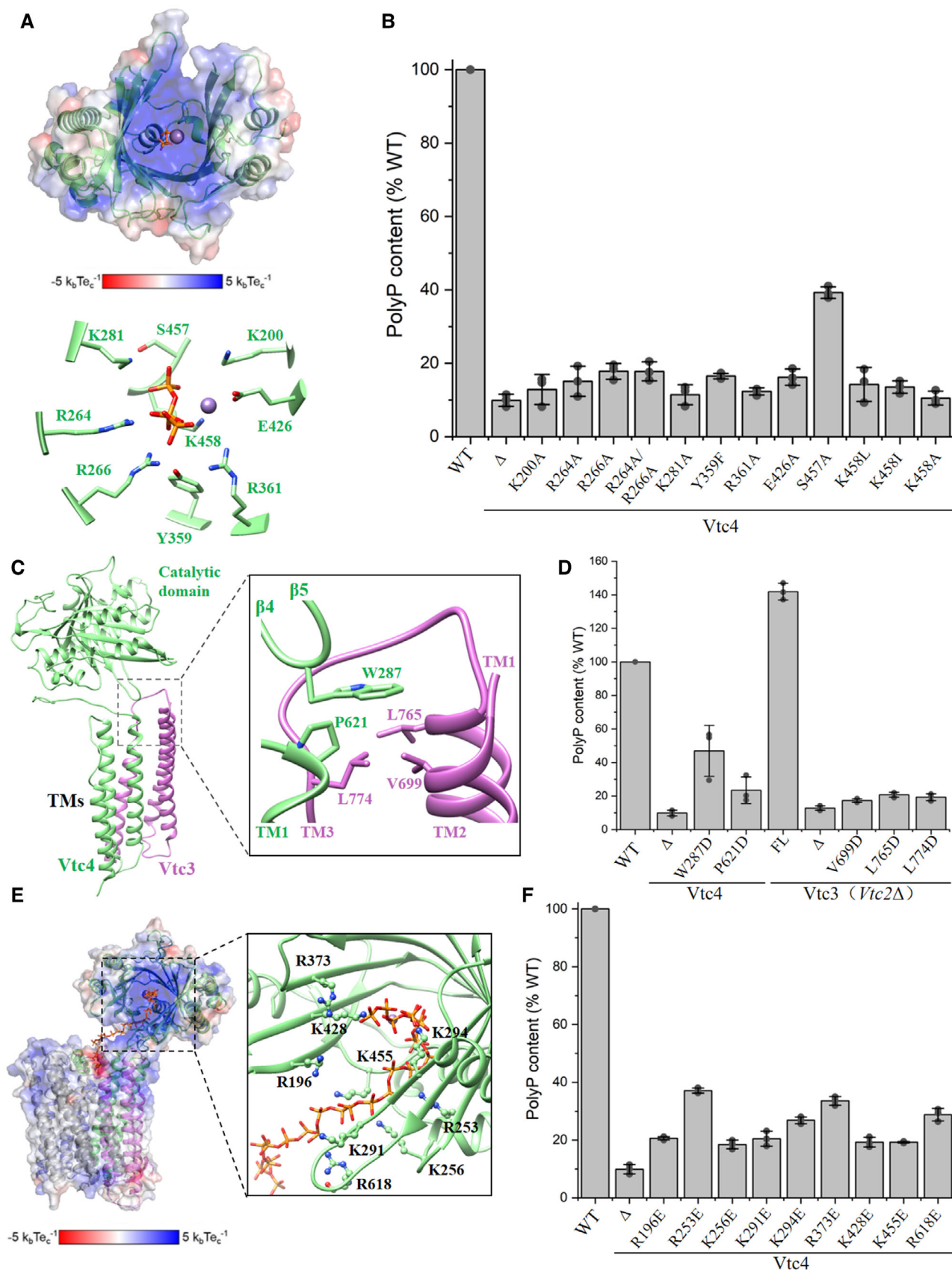


Figure 4.

Figure 4. Structural and functional data of the VTC complex reveal that polyP synthesis and transport are coupled.

- A Structure and electrostatic surface potential of the central domain of Vtc4. The triphosphate and Mn²⁺ are shown in orange and brown, respectively. Some key residues are shown.
- B Cellular polyP content of Vtc4p point mutants expressed under the control of their native promoters in the *vtc4Δ* background. Data show the mean ± s.d. (biological replicates *n* = 3).
- C Interactions between the β4-β5 loop of Vtc4 and the transmembrane domains of Vtc3 and Vtc4.
- D Cellular polyP content of *VTC4* and *VTC3* point mutants expressed under the control of their native promoters in the *vtc4Δ* and *vtc3Δ(vtc2Δ)* backgrounds, respectively. Data show the mean ± s.d. (biological replicates *n* = 3).
- E Superposition of the central domain of Vtc4 and the central domain of the polyP-bound Vtc4 (PDB: 3G3Q) structures. The structure of the central domain of polyP-bound Vtc4 is shown in blue. The polyP chains are shown in orange to overlap the triphosphates.
- F Cellular polyP content of *VTC4* point mutants expressed under the control of their native promoters in the *vtc4Δ* backgrounds. Data show the mean ± s.d. (biological replicates *n* = 3).

Source data are available online for this figure.

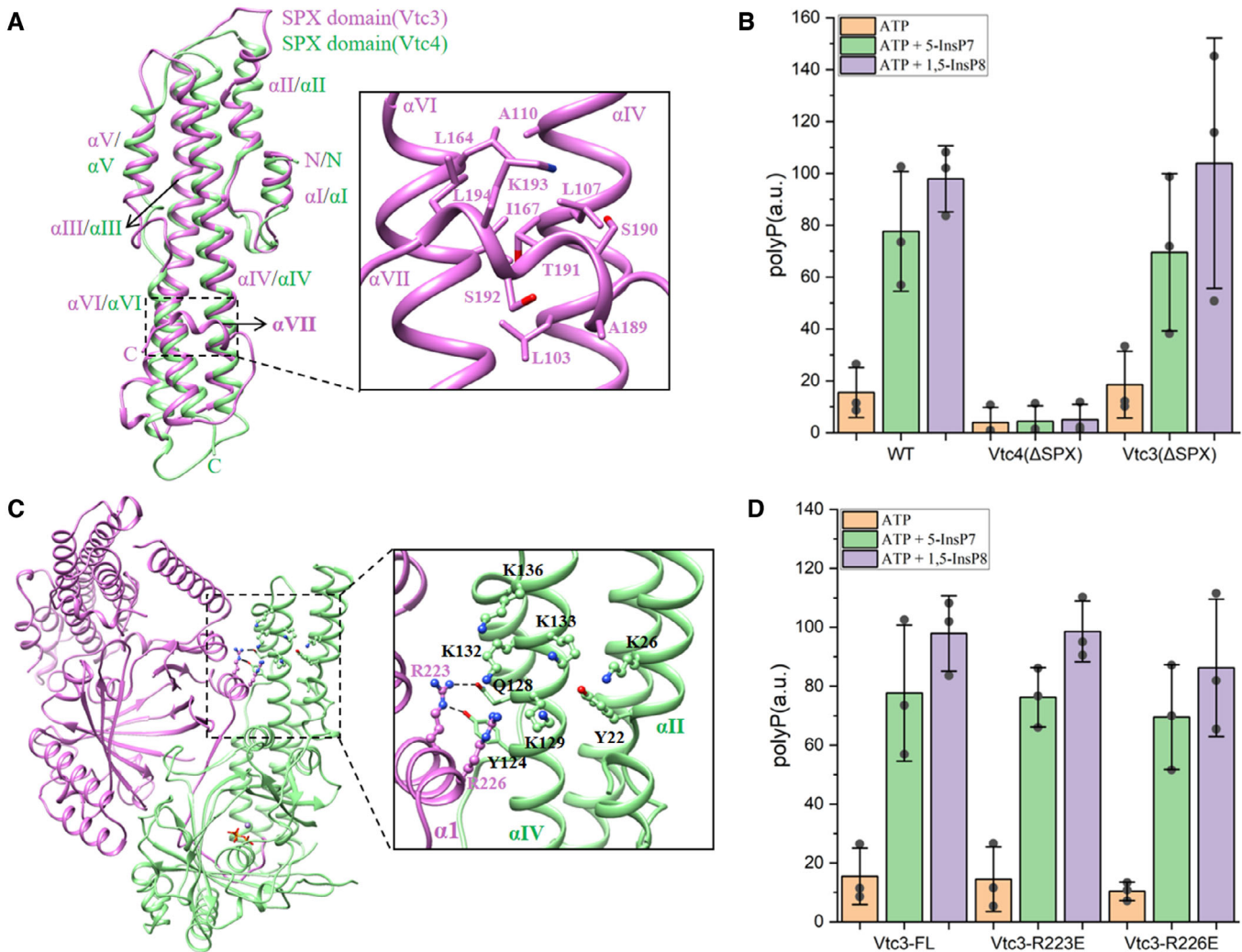


Figure 5. SPX domain of Vtc4 regulates polyP synthesis in a PP-InsPs-dependent manner.

- A Superposition of the SPX domain of Vtc4 and the SPX domain of Vtc3. The SPX domain of Vtc3 is shown in orchid, and the SPX domain of Vtc4 is shown in light green.
- B PolyP synthesis by isolated vacuoles carrying Vtc4(ΔSPX)/Vtc3/Vtc1 complex, Vtc4/Vtc3(ΔSPX)/Vtc1 complex or Vtc4/Vtc3/Vtc1 complex in the absence or presence of 1 μM 5-InsP₇ or 1,5-InsP₈ *in vitro*. The reaction system is detailed in [Materials and Methods](#). Data show the mean ± s.d. (biological replicates *n* = 3).
- C Two conserved arginine residues on Vtc3 potentially involved in regulation by PP-InsPs.
- D PolyP synthesis by isolated vacuoles carrying Vtc4/Vtc3(R223E)/Vtc1 complex, Vtc4/Vtc3(R226E)/Vtc1 complex or Vtc4/Vtc3/Vtc1 complex in the absence or presence of 1 μM 5-InsP₇ or 1,5-InsP₈ *in vitro*. The reaction system is detailed in [Materials and Methods](#). Data show the mean ± s.d. (biological replicates *n* = 3).

Source data are available online for this figure.

acidic residues and performed the polyP synthesis experiments on the purified mutant Vtc4/Vtc3/Vtc1 complexes (Appendix Fig S9A and B). Compared with the wild-type complex, both mutant complexes display significantly reduced polyP synthesis in the absence of stimulation by InsP₆, with a 50% reduced activity for the R226E mutant (Fig EV4B). However, addition of InsP₆ strongly stimulated the mutant complexes, reducing the difference to the wild-type complex to only 10–20% (Fig EV4B). Isolated vacuoles carrying the mutant Vtc4/Vtc3/Vtc1 complex also showed similar results to purified complexes, with the mutant R226E showed similar results as the purified complex (Fig 5D). Addition of 5-InsP₇ or 1,5-InsP₈ strongly enhanced the polyP synthesis activity (Fig 5D), leaving little difference between the substituted complexes and the wild type.

A regulatory loop of VTC3

An interesting aspect of the Vtc4/Vtc3/Vtc1 complex is the conformation and orientation of a loop between $\alpha 1$ and $\beta 2$ of the central domain of Vtc3. In comparison with Vtc4, this loop of Vtc3 is unusually long, containing over 60 amino acids (Appendix Fig S3). The N-terminal half of the loop (²²⁸LPALVYASVPNENDDFVDNLESD²⁵⁰), which is rich in acidic residues, forms of a nine-residue loop (²²⁸LPALVYASV²³⁶), a four-residue turn (²³⁷PNEN²⁴⁰), a five-residue loop (²⁴¹DDFVD²⁴⁵), and a five-residue turn (²⁴⁶NLESD²⁵⁰). It winds across the heterodimeric interface between the two central domains and the tunnel exit of the Vtc4 central domain, interacting with $\beta 1$, $\alpha 1$, $\beta 2$, $\beta 5$, $\alpha 4$, $\alpha 5$, and $\beta 7$ of Vtc4 (Fig 6A). The last five-residue turn loop (²⁴⁶NLESD²⁵⁰) of the loop is close to the triphosphate observed in the structure and forms multiple interactions with positively charged residues of Vtc4, including R196, R280, K281, K294, K300, R373, and K428, suggesting a regulatory role on polyP synthesis of this loop (Fig 6A).

In an effort to probe the regulatory role of the loop, we first generated a truncated form of Vtc3 by replacing this long loop (residues 234–292) with a short linker (GGSGGS) and performed polyP synthesis experiments on the purified mutant Vtc4/Vtc3/Vtc1 complex (Appendix Fig S10A and B). The mutant Vtc4/Vtc3/Vtc1 complex retained a slightly higher polyP synthesis activity than that of the wild-type complex, suggesting a potentially negative regulatory role of the loop (Fig 6B). Further, addition of InsP₆ enhanced polyP synthesis to similar degrees both for the mutant and wild-type Vtc4/Vtc3/Vtc1 complexes, even at low concentrations of ATP (Fig 6C). The moderate effect of deleting the long loop led us to probe another possibility, in which we noticed that the C-terminal half of the loop without visible EM density (²⁵¹VRVQPEARLNIGSKSNLSLSSDGNLNQDVEIGKSKSVIFPQSY²⁹²) contains a cluster of phosphorylation sites, suggesting possible regulation by phosphorylation. To mimic a nonphosphorylated or a phosphorylated state of the loop, we substituted six of its serine residues (S263, S265, S267, S269, S270, and S274) by either alanine or aspartate and performed the polyP synthesis experiments with vacuoles purified from respective mutants. In the absence of PP-InsPs, vacuoles carrying the alanine-substituted loop displayed more than 200% higher polyP synthesis activity *in vitro* than vacuoles from wild type, whereas the phospho-mimetic aspartate substituted form had a significantly reduced activity (Fig 6D). Addition of PP-InsPs significantly enhanced polyP synthesis of both nonphosphorylated and phospho-mimetic forms, conveying similar activity as for the wild-type form (Fig 6D). This is

consistent with a negative regulatory role of the loop, silencing the complex when P_i (and hence PP-InsPs) are low. This silencing role may be enhanced by its phosphorylation. When P_i becomes abundant, silencing may be overridden by the increase in PP-InsPs. The loop might thereby enhance the dynamic range over which VTC can be regulated, supporting a complete shut-down of polyP synthesis under P_i starvation while preserving the potential for full activation when P_i is abundant. Given that Vtc2 and Vtc3 share a same loop with high sequence identity (Appendix Fig S3), the loop of Vtc2 likely adopts the same conformation and orientation and performs similar regulatory function as the loop in Vtc3.

Mechanics of polyP channel gating

How the TM1 helices move to open the polyP channel of the VTC complex is a difficult question to answer in the absence of the open polyP channel structure. Nevertheless, the polyP channel in such a resting and fastened state provides valuable hints on conformational changes that may gate the polyP channel gating. First, the fivefold symmetry of the polyP channel is broken, as revealed by the two distorted pentagons by connecting the adjacent C α s of the two positively charged rings at the cytoplasmic vestibule of the VTC channel (Fig 7A). The inter-subunit interfaces are extensive and involve different subunits of the VTC channel. We define principal (+) and complementary (–) subunits and interfaces (Fig 7B), where the principal (+) interface is made up of TM1 and TM3 of the principal subunit, while the complementary (–) interface is made up of TM1 and TM2 of the complementary subunit (Fig 7B). We superimposed the principal subunit of all the five inter-subunit interfaces of the polyP channel, Vtc1(α)-Vtc1(β), Vtc1(β)-Vtc1(γ), Vtc1(γ)-Vtc3, Vtc3-Vtc4, and Vtc4-Vtc1(α) and observed that the two transmembrane domains forming the interface can have various relative positions, with Vtc1(β)-Vtc1(γ) and Vtc3-Vtc4 packing tightly, Vtc1(γ)-Vtc3 loosely, and Vtc1(α)-Vtc1(β) and Vtc4-Vtc1(α) in between (Fig 7B). Correspondingly, the Vtc3-Vtc4 interface buries the most (4,150 Å²) protein surface area from solvent, followed by Vtc1(β)-Vtc1(γ) (2,920 Å²), Vtc4-Vtc1(α) (2,870 Å²), and Vtc1(α)-Vtc1(β) (2,660 Å²) interfaces. The Vtc1(γ)-Vtc3 interface has the smallest buried surface area (2,350 Å²). This agrees with the observed asymmetry of the VTC channel. Several reasons can account for the altered relative positioning at the inter-subunit interfaces: Forces imposed by the latch-like, horizontal helix of Vtc4, and the constraint of interacting with the central domain of Vtc4. The important point is, however, that the inter-subunit interface is clearly flexible.

We also observed an unusual salt bridge among the mainly hydrophobic interactions, at the center of the inter-subunit interface. E30 and R83 of Vtc1 are strictly conserved among Vtc1, Vtc2, Vtc3, and Vtc4 from different species (Fig 7C). R83 from the principal (+) Vtc1 subunit forms a salt bridge with E30 of the complementary (–) Vtc1 subunit. The corresponding residues are E704 and R762 of Vtc3, and E628 and R681 of Vtc4 (Fig 7D). Similar salt bridges exist between Vtc3 and Vtc4, and Vtc4 and Vtc1(α). However, R83 of Vtc1(γ) and E704 of Vtc3 are separated by 8 Å, too far to form a salt bridge (Fig 7D). To confirm the importance of the observed inter-subunit salt bridge, we created 12-point mutants in the VTC complex and measured their cellular polyP content. All substitutions designed to disrupt the inter-subunit salt bridge by charge reversal or charge removal significantly reduced cellular polyP content

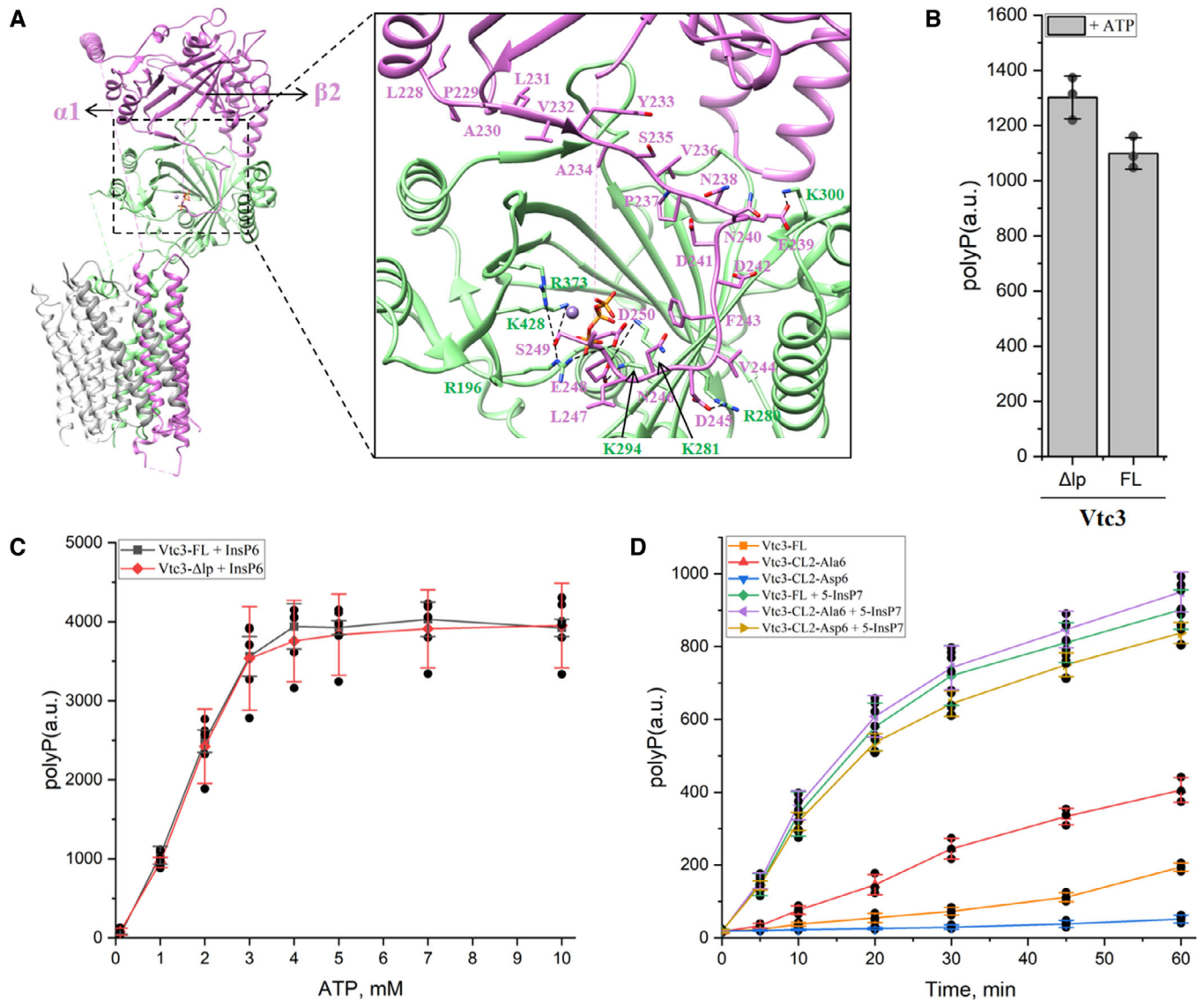


Figure 6. Structure and function of the regulatory loop of Vtc3.

A Structure of the regulatory loop of Vtc3. The loop is located between $\alpha 1$ and $\beta 2$ of Vtc3, and the loop sequence consists of ²²⁸LPALVYASVPNENDDFVDNLESD²⁵⁰. Interactions (dotted lines) are shown.

B Purified truncated Vtc4/Vtc3(Δ lp)/Vtc1 complexes synthesize polyP in the presence of ATP *in vitro*. Δ lp indicates that the regulatory loop of Vtc3 (residues 234–292) was replaced by a small linker (GGSGGS). The reaction system is detailed in [Materials and Methods](#). Data show the mean \pm s.d. (biological replicates $n = 3$).

C PolyP synthesis curves of purified endogenous Vtc4/Vtc3/Vtc1 and truncated Vtc4/Vtc3(Δ lp)/Vtc1 complexes at different ATP concentrations in the absence or presence of 10 mM InsP₆ *in vitro*. The reaction system is detailed in [Materials and Methods](#). Data show the mean \pm s.d. (biological replicates $n = 3$).

D PolyP synthesis by isolated vacuoles carrying Vtc4/Vtc3(CL2-Ala6)/Vtc1 complex, Vtc4/Vtc3(CL2-Asp6)/Vtc1 complex or Vtc4/Vtc3/Vtc1 complex in the absence or presence of 1 μ M 5-InsP₇ or 1.5-InsP₈ *in vitro*. The reaction system is detailed in [Materials and Methods](#). Data show the mean \pm s.d. (biological replicates $n = 3$).

Source data are available online for this figure.

(Fig 7E), indicating that the inter-subunit salt bridges are necessary for VTC complex function. To our surprise, substitution of E704 of Vtc3, which does not form an inter-subunit salt bridge in the structure, also significantly reduced cellular polyP content (Fig 7E). We hence speculate that E704 of Vtc3 might form such an inter-subunit salt bridge in another functional state of VTC, for example during VTC channel opening and transit of a polyP chain. Due to their role in VTC complex function, we term these salt bridges as inter-subunit “ionic locks.”

The flexible nature of the inter-subunit interface, together with the observation of inter-subunit “ionic locks,” suggests a plausible polyP channel gating mechanism. We assume that the polyP channel was captured in a resting state with the entrance nestled by a latch-like, horizontal helix of Vtc4. The asymmetrical nesting of this horizontal helix of Vtc4 at the entrance of the channel imposes forces asymmetrically, resulting in different relative positioning at the inter-subunit interfaces. Three loosely packing inter-subunit interfaces, together with two tightly packing ones, render the TM1

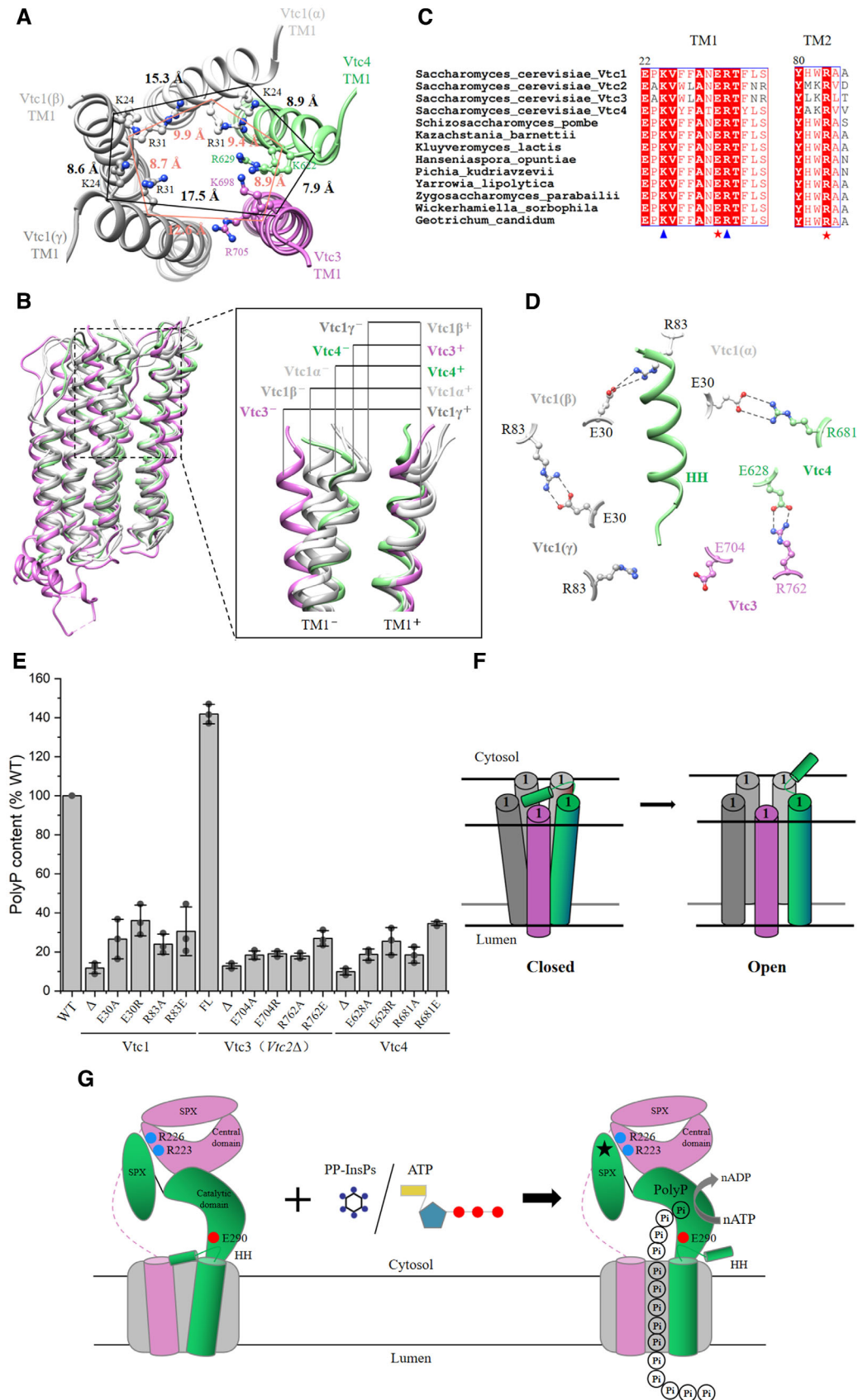


Figure 7.

Figure 7. Asymmetric polyP channel and inter-subunit ionic locks.

- A Asymmetry in the channel at the level of the activation and desensitization gates. Residues at the polyP selectivity filter are shown in ball-and-stick representation. Distance between C α of polyP selectivity filter residues is given in Å.
- B Superposition of the principal subunits of all the five inter-subunit interfaces of the polyP channel.
- C Sequence alignment of Vtc1, Vtc2, Vtc3 and Vtc4 from different species. Protein sequence numbers in NCBI: *Saccharomyces cerevisiae*_Vtc1 (ID: NP_010995.1); *Saccharomyces cerevisiae*_Vtc2 (ID: KZV11596.1); *Saccharomyces cerevisiae*_Vtc3 (ID:KZV07497.1); *Saccharomyces cerevisiae*_Vtc4 (ID:QHB096.08.1); *Schizosaccharomyces pombe* (ID:NP_595683.1); *Kazachstania barnettii* (ID:XP_041404278.1); *Kluyveromyces lactis* (ID: QEU59996.1); *Hanseniaspora opuntiae* (ID: OEJ89736.1); *Pichia kudriavzevii* (ID:ONH77772.1); *Yarrowia lipolytica* (ID: QNP96953.1); *Zygosaccharomyces parabolii* (ID:AQZ10220.1); *Wickerhamiella sorbophila* (ID: XP_024663738.1); *Geotrichum candidum* (ID: CDO55024.1). Triangles and stars indicate key conserved amino acids, respectively.
- D Multiple pairs of conserved salt bridges are formed at the inter-subunit interface of the VTC complex. R83 of Vtc1(γ) and E704 of Vtc3 are separated by 8 Å, too far to form a salt bridge.
- E Cellular polyP content of *VTC4*, *VTC3* and *VTC1* point mutants expressed under the control of their native promoters in the *vtc4 Δ , *vtc3 Δ (*vtc2 Δ) and *vtc1 Δ backgrounds, respectively. Δ indicates that the entire subunit was knocked out. FL indicates full length, indicating that the subunit has not been modified in any way. Data show the mean \pm s.d. (biological replicates $n = 3$).****
- F A model of the putative polyP channel gating mechanism. The schematic drawing illustrates conformational changes of the polyP channel switching between closed and open states. The number 1 represents the TM1 of each subunit of the VTC complex.
- G A model of the activation mechanism of the VTC complex. Schematic of the Vtc4/Vtc3/Vtc1 complex. Subunits are colored. The three subunits of Vtc1 are shown in gray. Key amino acids are highlighted. The stars represent the binding sites of PP-InsPs or ATP.

Source data are available online for this figure.

helices tapering from the cytosolic side toward the intravacuolar side, generating a narrow point that might serve as a gate. The inter-subunit “ionic locks” may hold the subunits together. During opening of the polyP channel, the horizontal helix latch is lifted, and the subunits are pulled together by the “ionic locks,” possibly resulting in the formation of all five “ionic locks” between subunits. In this state, the TM1 helices might tilt inwards at the cytosolic side and outwards at the intravacuolar side, thus opening the channel (Fig 7F).

Discussion

The observed central domain of Vtc4 exists in a polyP polymerase “off” state

Three lines of evidence lead us to believe that the observed central domain of Vtc4 in our cryo-EM structure is in a polyP polymerase “off” state. First, polyP synthesis and the immediate translocation of polyP into the vacuole are coupled (Gerasimaite et al, 2014), and our structure of the Vtc4/Vtc3/Vtc1 complex supports such coupling. Given that the polyP channel in our structure is in a resting state, it is then reasonable to assume that also the polymerase is in the “off” state. Second, no polyP product was observed in the cryo-EM structure of the whole Vtc4/Vtc3/Vtc1 complex. This should in principle be possible because active Vtc4 central domain, synthesizing polyP from ATP, could be crystallized with its product bound, providing a putative polymerase “on” state (Hothorn et al, 2009). Third, structural comparison revealed that the β 4- β 5 loop of the central domain of Vtc4 adopts a different conformation between the crystal structure of the polyP-containing central domain of Vtc4 alone (Hothorn et al, 2009) and the cryo-EM structure of the whole Vtc4/Vtc3/Vtc1 complex (Fig EV5A). This suggests a structural transition between the putative active and inactive states. In line with this interpretation, the β 4- β 5 loop of the central domain of Vtc4 is very sensitive to mutagenesis. Substitutions in this region abolished polyP synthesis *in vitro* (E290G, E290A, and E290R) and *in vivo* (R284A/E285A/D286A) (Fig EV5B and C).

The activation mechanism of the VTC complex

The data presented here have allowed us to elucidate a possible activation mechanism of the VTC complex. We suppose that the VTC complex exists in equilibrium between an inactive and active state. ATP and the inositol-based signaling molecules activate the VTC complex. The Vtc4/Vtc3/Vtc1 structure was captured in an inactive state, with a resting state polyP channel and an “off” state polyP polymerase. How might the VTC complex convert the free energy of ATP binding, or the binding of the inositol-based signaling molecules to turn “on” the polyP polymerase, and open the polyP channel? To address this question, we superimposed the structures of isolated SPX domains (SPX^{CtVtc4}-InsP₆ (PDB ID: 5IJJ), or the SPX^{CtVtc4}-InsP₆ (PDB ID: 5IJP); Wild et al, 2016) to the SPX domain of Vtc4 of the intact VTC complex, and observed that the InsP₆ bound on the SPX domain is close to Vtc3 (Fig EV5D). The SPX domain harbors a large, positively charged surface able to interact with phosphate-containing inositol ligands but showing little specificity and selectivity at the level of binding (Wild et al, 2016). One can imagine that a phosphate-containing ligand, such as ATP, 5-InsP₇, or 1,5-InsP₈, binds in the cleft between the large, positively charged surface of the SPX domain of Vtc4 and the α 1 helix of the central domain of Vtc3 and causes the domains to move relative to each other, thus inducing conformational change that turns “on” the polyP polymerase, followed by the opening of the polyP channel. In addition, it is worth noting that the binding affinity of phosphate-containing ligands to SPX domain gradually increases from P_i, pyrophosphate (PP_i), triphosphate (PPP_i), to InsP₆, with a 20-fold lower K_d value of InsP₆ than that of PPP_i (Wild et al, 2016). This allowed us to propose a simplified model of the regulation of the VTC complex (Fig 7G). The VTC complex contains a polyP polymerase, a polyP channel and a regulatory cleft, and exists in equilibrium between inactive and active states. The high apparent K_m value of VTC for ATP might be an additional mechanism to reduce VTC activity in situations where P_i is abundant but the cells cannot generate sufficient ATP to drive the conversion of large amounts of P_i into polyP. Then, the high K_m would provide an inbuilt mechanism to reduce polyP synthesis, which is a strong consumer of ATP but dispensable for survival under such conditions. PP-InsPs might

serve as high-affinity stimulatory ligands when ATP and P_i are abundant. Also the synthesis of InsPPs itself is probably impacted by the ATP concentration, because both the InsP₆ kinases and PPIP kinases, which synthesize 5-InsP₇ and 1,5-InsP₈, have high K_m values for ATP (Voglmaier *et al.*, 1996; Nair *et al.*, 2018), which are close to the ATP concentrations in the cytosol. Thus, the VTC complex may integrate information about the ATP and phosphate status of the cell at two levels. Such control at multiple levels may be justified by the fact that VTC is a powerful phosphate pump: Powerful enough to push the cells into phosphate starvation when overactivated (Desfougeres *et al.*, 2016; Austin & Mayer, 2020); and capable of accumulating hundreds of millimolar of P_i units in the form of polyP (Urech *et al.*, 1978), which must consume even higher concentrations of ATP.

Materials and Methods

Yeast strains and plasmids

The strains and oligonucleotides used in this study are summarized in Appendix Tables S2 and S3, respectively. The protease-deficient *S. cerevisiae* BJ2168 (MATa: leu2-3, trp1-289, ura3-52, prb1-1,122, pep4-3, prc1-407, and gal2) was used as a host strain. The modified TAP tag (6His-TEV-Protein A, named TAPm tag) or the strep tag was inserted at the C terminus of Vtc2 or Vtc3 by a homologous recombination-based method (Funakoshi & Hochstrasser, 2009). Based on the above methods, we constructed Vtc2-TAPm, Vtc3-TAPm, and Vtc3(Δ C24)-TAPm single-tag strains, as well as Vtc2-TAPm/Vtc3-Strep and Vtc2-Strep/Vtc3-TAPm dual-tag strains.

Single subunit knockout strains Vtc1 Δ , Vtc2 Δ , Vtc3 Δ , and Vtc4 Δ were prepared using a plasmid pYM27-kanMX in the BJ2168 strain. The kanMX gene replaces the VTC gene behind the promoter of the corresponding subunit. Double subunits knockout strain Vtc2 Δ and Vtc3 Δ were prepared using a plasmid p426-URA3 in the Vtc3 Δ strain.

The genes of Vtc1, Vtc2, Vtc3, and Vtc4 were cloned into plasmid p426-URA3 for various site-directed mutagenesis. Vtc1 point mutants were expressed from p426-URA3 plasmid integrated into the genome behind the Vtc1 promoter of a VTC1::kanMX strain. Similarly, Vtc2, Vtc3, and Vtc4 point mutants were performed in the same way.

Saccharomyces cerevisiae Ppx1 was cloned into pET28a (kanamycin selection) vector and transferred to BL21 (DE3) for expression.

Purification of the endogenous wild-type and mutant VTC complexes

Yeast cells were cultured in YPD (2% peptone, 1% yeast extract, and 2% glucose) medium for 18 h. The cells were collected by centrifugation at 4,625 g at 4°C. The collected cells were resuspended in lysis buffer containing 25 mM Hepes-NaOH (pH 7.4), 150 mM NaCl, and 1 mM EDTA and supplemented with a protease inhibitor cocktail (2 μ g/ml DNase I, 1 μ g/ml pepstatin, 1 μ g/ml leupeptin and 1 μ g/ml aprotinin, and 1 mM PMSF) and then were lysed using a high-pressure homogenizer at 1,000 bar for 5 cycles. After lysis, cell debris was pelleted by centrifugation at 8,000 g for 10 min. The supernatant was subjected to centrifugation in a Ti45 rotor

(Beckman) at 186,000 g at 4°C for 1 h. The pelleted membranes were resuspended with a Dounce homogenizer in buffer A containing 25 mM Hepes-NaOH (pH 7.4), 150 mM NaCl, 1 mM EDTA, 1 mM MgCl₂, 1 mM MnCl₂, 1 mM PMSF, 2% n-Dodecyl- β -D-Maltopyranoside (DDM, Anatrace), and 0.2% cholesteryl hemisuccinate (CHS, Sigma Aldrich). After incubation at 4 °C for 3 h, the mixture was centrifuged at 38,758 g for 30 min to remove insolubilized membrane. The supernatant was incubated with 600 μ l IgG resin for 3 h. The beads were washed with 30 ml buffer B (25 mM Hepes-NaOH (pH 7.4), 150 mM NaCl, 1 mM MgCl₂, 1 mM MnCl₂, 0.1% digitonin), and the complex was eluted with buffer B containing 0.15 mg/ml TEV protease. The complex was concentrated and further purified by size-exclusion chromatography on a Superose 6 10/300 Increase column, equilibrated with buffer B. Peak fractions were pooled and concentrated to 8 mg/ml for cryo-EM analysis.

Cryo-EM grid preparation and data collection

For the cryo-EM grids preparation, 3 μ l purified Vtc4/Vtc3/Vtc1 complex at a concentration of approximately 8 mg/ml was applied, respectively, to glow-discharged holey carbon EM grids (CryoMatrix Amorphous alloy film R1.2/1.3, 300 mesh). The grids were blotted for 3 s with a blot force of 0 and then plunged into liquid ethane using a FEI Vitrobot Mark IV (Thermo Fisher Scientific) at 4°C and 100% humidity. The cryo-EM grids were subsequently transferred into a 300 kV Titan Krios microscope (Thermo Fisher Scientific) equipped with a Gatan K3 direct electron detector and a BioQuantum energy filter operated at a slit width of 20 eV. Micrographs were automatically collected by EPU in super-resolution mode with a pixel size of 0.4255 Å. Each micrograph was comprised of 40 frames with a total exposure time of 2.5 s and total dose of 54 electrons per Å². The defocus range for each micrograph was set from -1.0 to -1.5 μ m.

Cryo-EM data processing

The collected movie stacks were summed and corrected for beam-induced motion using MotionCor2 (Zheng *et al.*, 2017) with a binning factor of 2. Gctf (Zhang, 2016) was used for estimating contrast transfer function (CTF) parameters for each micrograph. And the following processing steps including particle picking, 2D classification, 3D classification, 3D auto-refine, CTF refinement and polishing were all performed using RELION-3.1.1 (Zivanov *et al.*, 2020). Local resolution map was estimated using RELION. All 3D density maps were displayed using UCSF Chimera (Pettersen *et al.*, 2004).

For the Vtc4/Vtc3/Vtc1 complex, 3,871 and 3,493 micrographs were collected separately. And a total of 1,641,408 and 1,764,870 particles were auto-picked and subjected to 2D classification and 3D classification individually. After that, good classes showed clear features were combined from two datasets including 1,542,410 particles and subjected to another round of 3D classification. And two best-resolved classes were chosen and combined containing 1,042,873 particles for 3D refinement, CTF refinement, and polishing. The final refinement generated a map with a global resolution of 3.06 Å. And signal subtract was used for a more detailed feature and higher resolution map of transmembrane region.

Cryo-EM model building, refinement, and validation

The initial templates of Vtc1, Vtc3, and Vtc4 were generated using AlphaFold2 (Jumper et al, 2021). The transmembrane domain, similar catalytic domain and SPX domain of Vtc3 and transmembrane domain, catalytic domain and SPX domain of Vtc4 were cut out and separately rigid body fitted into cryo-EM density map using Chimera (Pettersen et al, 2004). Then three copies of Vtc1 were docked into the remaining density map. The initial fitting of Vtc4/Vtc3/Vtc1 complex was confirmed by high agreement of secondary structural features between the predicted 3D models and the cryo-EM density map. Polyphosphate and POV coordinates and geometry restraints were generated using a phenix.elbow (Adams et al, 2010) and fitted into density map. All the models were manual adjusted and rebuild using Coot (Emsley & Cowtan, 2004), followed by several round of real-space refinement in PHENIX (Adams et al, 2010) and manual adjustment in COOT (Emsley & Cowtan, 2004). The final model statistics were validated and provided by MolProbity (Williams et al, 2018) and summarized in Appendix Table S1. Structural figures were prepared using Chimera (Pettersen et al, 2004).

Purification of recombinant ScPpx1

Escherichia coli BL21(DE3) cells were transfected with ScPpx1 plasmid and were grown in LB medium containing 50 µg/ml Kanamycin at 37°C. 0.4 mM IPTG was added when OD600 reached 0.6. The cells were transferred to 16°C and cultured for 18 h before harvesting. Cell pellets were resuspended in lysis buffer containing 50 mM Hepes-NaOH (pH 7.4), 300 mM NaCl and disrupted by sonication. After lysis, cell debris was removed by centrifugation at 38,758 g for 30 min. The supernatant was incubated with 2 ml Ni-NTA resin for 30 min. The beads were washed with 30 ml lysis buffer plus 20 mM imidazole, followed by a second wash with 30 ml of lysis buffer plus 50 mM imidazole. The protein was eluted with lysis buffer plus 250 mM imidazole. The eluted protein was dialyzed against 50 mM Hepes-NaOH (pH 7.4), 150 mM NaCl to remove imidazole. Dialyzed protein was concentrated using an Amicon Ultra concentrator (30 kDa MWCO, Millipore) and aliquoted into 100 µl amounts and stored at -80°C.

Detection of PolyP content *in vivo*

Yeast cells (including wild-type strains, knockout strains, and mutant strains) were grown overnight in YPD medium. The yeast cultures were first diluted to an OD600 value of 1, and the yeast cells were then collected from 2 ml of each culture by centrifugation at 4,625 g for 5 min.

PolyP extraction and purification are based on an improved method (Bru et al, 2016a). The cell pellet was resuspended with 400 µl of AE buffer (50 mM sodium acetate (pH 5.3), 10 mM EDTA) at 4°C, transferred to a screw cap tube containing 300 µl phenol and 40 µl 10% SDS, mixed by inversion 4 times, vortexed 5 s to homogenize, incubated at 65°C for 10 min, and chilled for 2 min on ice. The tube was further added 300 µl chloroform, mixed by inversion 4 times, vortexed 5 s to homogenize, and centrifuged at room temperature for 2 min at 23,446 g. The top aqueous phase was transferred to a prepared 1.5 ml screw cap tube containing 350 µl chloroform, mixed by inversion 4 times, vortexed 5 s to homogenize, and

centrifuged at room temperature at 23,446 g for 2 min. The aqueous phase was then transferred to a new 1.5 ml microcentrifuge tube, added 2 µl of RNase A (10 mg/ml) and 2 µl of DNase I (10 mg/ml), incubated at 37°C for 1 h, transferred to a pre-cold 1.5 ml microcentrifuge tube containing 1 ml of absolute ethanol and 40 µl of 3 M sodium acetate (pH 5.3), left at -20°C for 3 h to precipitate polyP, and centrifuged for 20 min at 23,446 g at 4°C. The supernatant was discarded. The precipitant was further washed with the addition of 500 µl of 70% ethanol, followed by centrifugation at 23,446 g at 4°C for 10 min, and with the supernatant discarded. The tube was left open to dry the small translucent-white polyP pellet at room temperature for 10 min or until the pellet is completely dry. Finally, the polyP was resuspended in 50 µl of deionized water. The polyP sample can be directly measured or stored at -20°C.

The purified polyP samples were measured by Malachite Green Phosphate Assay Kits (Sigma, POMG-25H). First, PolyP needs to be degraded into P_i by the polyphosphatase Ppx1. A 50 µl reaction system containing 5 µl PolyP, 0.5 µg Ppx1 and reaction buffer (50 mM Hepes-NaOH, pH 7.4, 150 mM NaCl) was left at 37°C for 1 h. The Malachite Green Phosphate Assay Kit is based on quantification of the green complex formed between Malachite Green, molybdate and free orthophosphate. The rapid color formation from the reaction can be conveniently measured on a spectrophotometer (600–660 nm). Standard phosphate was used for assay calibration.

PolyP synthesis by purified VTC complex in the absence or presence of InsP₆

PolyP synthesis was assayed in 15 µl samples consisting of reaction buffer (25 mM Hepes-NaOH (pH 7.4), 150 mM NaCl, 1 mM MgCl₂, 1 mM MnCl₂, 0.1% digitonin), 5 mM ATP and 6 µg purified endogenous proteins (Vtc4/2/1 complex, and Vtc4/3/1 complex). When indicated, 10 mM InsP₆ had been added. The entire reaction was maintained at 4°C for 1 h, and the reaction was terminated with the addition of the stop buffer (25 mM Hepes-NaOH (pH 7.4), 150 mM NaCl, 0.1% digitonin, 15 mM EDTA, 15 µM DAPI) until the total volume reached 200 µl. The addition of EDTA chelated the metal ions and quenched the catalytic activity of the VTC complex. DAPI can form a complex with synthetic polyP, allowing the measurement of the production of polyP based on the characteristic fluorescence emission of DAPI-polyP complex at 550 nm. A total of 200 µl of the sample were transferred into a black 96-well plate, and fluorescence was measured with a SPECTRAMax GEMINI XS fluorescence plate reader (Molecular Devices) using λ_{exc} = 415 nm, λ_{em} = 550 nm at 27°C (Gerasimaite et al, 2014).

PolyP detection by PAGE gel

In vivo purified polyP or *in vitro* synthesized polyP was mixed with one volume of 2× TBE-Urea sample buffer (50% urea, 2× TBE, 0.25% xylene cyanol, 0.25% bromophenol blue). The sample was resolved electrophoretically using a 12% polyacrylamide gel (29:1 acrylamide /bis-acrylamide) containing 7 M urea in TBE buffer pH 8.3, at 250 V/h at 4°C for 2.5 h. The dimensions of the gel were 200 mm height, 200 mm wide, and 1.5 mm thick. The gel was stained by soaking it in the staining solution (25% methanol, 5% glycerol, 2 µg/ml DAPI, 50 mM Tris pH 10.5) for 30 min, and destained by soaking it in destaining solution (25% methanol, 5%

glycerol, 50 mM Tris pH 10.5) for 1 h. Finally, the gel was exposed to 254 nm UV light in Syngene G-BOX trans-illuminator to visualize the polyP.

Western blot detection of the interaction between Vtc2 and Vtc3

The Vtc2-TAPm/Vtc3-Strep and Vtc2-Strep/Vtc3-TAPm strains were collected, followed by disruption, membrane solubilization with detergent, and centrifugation. The supernatant was incubated with IgG beads for 2 h, followed by washing, and the protein was eluted by TEV protease. Add reducing SDS sample buffer to the samples and incubate at 75°C for 5 min. Vtc2 and Vtc3 were detected using anti-His and anti-Strep antibodies.

Chemical synthesis and analysis of PP-InsPs

Chemical synthesis and analysis of 5-InsP₇ and 1,5-InsP₈ were performed as described previously (Pavlovic *et al*, 2016).

Isolation of vacuoles

Vacuoles were essentially prepared as described (D'Agostino *et al*, 2018). The cells were grown in 1 liter of YPD medium at 30°C overnight and harvested at an OD₆₀₀ of 0.6–1.3. A total of 600 ml of culture were centrifuged (2 min, 3,900 g). Cells were resuspended in 50 ml of 0.1 M Tris–HCl pH 8.9, 10 mM DTT, incubated at 30°C for 7 min in a water bath and collected by centrifugation. Cells were resuspended in 15 ml of spheroplasting buffer (50 mM potassium phosphate pH 7.5, 600 mM sorbitol in YPD with 0.2% glucose), 3,000–4,500 units of lyticase (Reese *et al*, 2005) were added, and cells were incubated for 26 min at 30°C in a water bath. Spheroplasts were collected by centrifugation (3 min, 3,400 g, 4°C) and gently resuspended in 15 ml of 15% Ficoll 400 in PS buffer (10 mM PIPES/KOH pH 6.8, 200 mM sorbitol). Spheroplasts were lysed by adding DEAE-dextran to a concentration of 7 mg/l and incubated (2 min, 0°C, then 2 min, 30°C). Samples were chilled, transferred into SW41 tubes, and overlaid with 2.5 ml of 8% Ficoll 400, 3.5 ml of 4% Ficoll 400, and 1.5 ml of 0% Ficoll 400 (all in PS buffer). After centrifugation (150,000 g, 90 min, 4°C), vacuoles were harvested from the 0–4% interface. When isolating vacuoles from proteolytically competent strains, 1 mM PMSF and 1X protease inhibitor cocktail (1X PIC—100 mM pefabloc SC, 100 ng/ml leupeptin, 50 mM O-phenanthroline and 500 ng/ml pepstatin A) were included in all buffers, starting from the spheroplasting step. Vacuole amounts were determined by protein content, using the Bradford assay with fatty-acid-free BSA as standard.

PolyP synthesis by isolated vacuoles

PolyP synthesis was assayed in 100-μl samples consisting of reaction buffer (10 mM PIPES/KOH pH 6.8, 150 mM KCl, 0.5 mM MnCl₂, 200 mM sorbitol) and ATP-regenerating system (ATP-RS—1 mM ATP-MgCl₂, 40 mM creatine phosphate and 0.25 mg/ml creatine kinase). The reactions were started by adding 2 μg of purified vacuoles, and the samples were incubated at 27°C, followed by the addition of 200 μl of stop solution (12 mM EDTA, 0.15% Triton X-100 and 15 μM DAPI) in dilution buffer (10 mM PIPES/KOH pH 6.8, 150 mM KCl, 200 mM sorbitol). This threefold dilution with EDTA-

containing buffer did not only stop nucleotide hydrolysis but also resulted in faster development of DAPI–polyP fluorescence. Given that DAPI is membrane impermeable, dissolving the membranes with detergent was required in order to detect the entire polyP pool. A total of 240 μl of the sample were transferred into a black 96-well plate, and fluorescence was measured with a SPECTRAMax GEMINI XS fluorescence plate reader (Molecular Devices) using λ_{ex} = 415 nm, λ_{em} = 550 nm (cutoff = 530 nm) at 27°C. Fluorescence was read every 1–2 min until the signal was stable. Experiments were repeated with at least three independent vacuole preparations. Values are presented as the mean ± s.d.

Data availability

The structure coordinates and cryo-EM density maps have been deposited in the protein data bank under accession number 8I6V (<http://www.rcsb.org/pdb/explore/explore.do?structureId=8I6V>) and EMD-35208 (<http://www.ebi.ac.uk/pdbe/entry/EMD-35208>).

Expanded View for this article is available [online](#).

Acknowledgements

This work was supported in part by the Ministry of Science and Technology (2020YFA0908500 to SY and 2020YFA0908400 to SW), the National Natural Science Foundation of China (31971127 to SY and 31900930 to SW), China Postdoctoral Science Foundation (2020M672434 to SW), and the Fundamental Research Funds for the Central Universities (to SY); the ERC (788442 to AM); the SNSF (CRSII5_170925 to AM); and the DFG (CIBSS—EXC-2189—Project ID 390939984 to HJJ).

Author contributions

Sheng Ye: Conceptualization; supervision; funding acquisition; validation; visualization; writing – original draft; project administration; writing – review and editing. **Wei Liu:** Data curation; formal analysis; writing – original draft. **Jiening Wang:** Data curation. **Véronique Comte-Miserez:** Data curation. **Mengyu Zhang:** Data curation. **Xuejing Yu:** Data curation. **Qingfeng Chen:** Data curation. **Andreas Mayer:** Conceptualization; data curation; funding acquisition; writing – review and editing. **Shan Wu:** Conceptualization; data curation; funding acquisition; writing – original draft. **Henning Jacob Jessen:** Resources; funding acquisition.

Disclosure and competing interests statement

The authors declare that they have no conflict of interest.

References

- Adams PD, Afonine PV, Bunkoczi G, Chen VB, Davis IW, Echols N, Headd JJ, Hung LW, Kapral GJ, Grosse-Kunstleve RW *et al* (2010) PHENIX: a comprehensive python-based system for macromolecular structure solution. *Acta Crystallogr D Biol Crystallogr* 66: 213–221
- Akiyama M, Croke E, Kornberg A (1992) The polyphosphate kinase gene of *Escherichia coli*. Isolation and sequence of the ppk gene and membrane location of the protein. *J Biol Chem* 267: 22556–22561
- Ansermet C, Moor MB, Centeno C, Auberson M, Hu DZ, Baron R, Nikolaeva S, Haenzi B, Katanaeva N, Gautschi I *et al* (2017) Renal Fanconi syndrome and Hypophosphatemic rickets in the absence of Xenotropic and

- Polytropic retroviral receptor in the nephron. *J Am Soc Nephrol* 28: 1073–1078
- Austin S, Mayer A (2020) Phosphate homeostasis – a vital metabolic equilibrium maintained through the INPHORS signaling pathway. *Front Microbiol* 11: 1367
- Azevedo C, Livermore T, Saiardi A (2015) Protein polyphosphorylation of lysine residues by inorganic polyphosphate. *Mol Cell* 58: 71–82
- Azevedo C, Singh J, Steck N, Hofer A, Ruiz FA, Singh T, Jessen HJ, Saiardi A (2018) Screening a protein Array with synthetic biotinylated inorganic polyphosphate to define the human PolyP-ome. *ACS Chem Biol* 13: 1958–1963
- Bentley-DeSousa A, Holinier C, Moteshareie H, Tseng YC, Kajjo S, Nwosu C, Amodeo GF, Bondy-Chorney E, Sai Y, Rudner A et al (2018) A screen for candidate targets of lysine Polyphosphorylation uncovers a conserved network implicated in ribosome biogenesis. *Cell Rep* 22: 3427–3439
- Bondy-Chorney E, Abramchuk I, Nasser R, Holinier C, Denoncourt A, Baijal K, McCarthy L, Khacho M, Lavallee-Adam M, Downey M (2020) A broad response to intracellular long-chain polyphosphate in human cells. *Cell Rep* 33: 108318
- Bru S, Jimenez J, Canadell D, Arino J, Clotet J (2016a) Improvement of biochemical methods of polyP quantification. *Microb Cell* 4: 6–15
- Bru S, Martinez-Lainez JM, Hernandez-Ortega S, Quandt E, Torres-Torronteras J, Marti R, Canadell D, Arino J, Sharma S, Jimenez J et al (2016b) Polyphosphate is involved in cell cycle progression and genomic stability in *Saccharomyces cerevisiae*. *Mol Microbiol* 101: 367–380
- Cohen A, Perzov N, Nelson H, Nelson N (1999) A novel family of yeast chaperons involved in the distribution of V-ATPase and other membrane proteins. *J Biol Chem* 274: 26885–26893
- D'Agostino M, Risselada HJ, Endter LJ, Comte-Miserez V, Mayer A (2018) SNARE-mediated membrane fusion arrests at pore expansion to regulate the volume of an organelle. *EMBO J* 37: e99193
- Desfougeres Y, Gerasimaite RU, Jessen HJ, Mayer A (2016) Vtc5, a novel subunit of the vacuolar transporter chaperone complex, regulates polyphosphate synthesis and phosphate homeostasis in yeast. *J Biol Chem* 291: 22262–22275
- Docampo R, Huang G (2016) Acidocalcisomes of eukaryotes. *Curr Opin Cell Biol* 41: 66–72
- Emsley P, Cowtan K (2004) Coot: model-building tools for molecular graphics. *Acta Crystallogr D Biol Crystallogr* 60: 2126–2132
- Funakoshi M, Hochstrasser M (2009) Small epitope-linker modules for PCR-based C-terminal tagging in *Saccharomyces cerevisiae*. *Yeast* 26: 185–192
- Gerasimaite R, Mayer A (2016) Enzymes of yeast polyphosphate metabolism: structure, enzymology and biological roles. *Biochem Soc Trans* 44: 234–239
- Gerasimaite R, Sharma S, Desfougeres Y, Schmidt A, Mayer A (2014) Coupled synthesis and translocation restrains polyphosphate to acidocalcisome-like vacuoles and prevents its toxicity. *J Cell Sci* 127: 5093–5104
- Gerasimaite R, Pavlovic I, Capolicchio S, Hofer A, Schmidt A, Jessen HJ, Mayer A (2017) Inositol pyrophosphate specificity of the SPX-dependent polyphosphate polymerase VTC. *ACS Chem Biol* 12: 648–653
- Gray MJ, Wholey WY, Wagner NO, Cremers CM, Mueller-Schickert A, Hock NT, Krieger AG, Smith EM, Bender RA, Bardwell JCA et al (2014) Polyphosphate is a primordial chaperone. *Mol Cell* 53: 689–699
- Hassanian SM, Dinarvand P, Smith SA, Rezaie AR (2015) Inorganic polyphosphate elicits pro-inflammatory responses through activation of the mammalian target of rapamycin complexes 1 and 2 in vascular endothelial cells. *J Thromb Haemost* 13: 860–871
- Hoac B, Kiffer-Moreira T, Millan JL, McKee MD (2013) Polyphosphates inhibit extracellular matrix mineralization in MC3T3-E1 osteoblast cultures. *Bone* 53: 478–486
- Holmstrom KM, Marina N, Baev AY, Wood NW, Gourine AV, Abramov AY (2013) Signalling properties of inorganic polyphosphate in the mammalian brain. *Nat Commun* 4: 1362
- Hothorn M, Neumann H, Lenherr ED, Wehner M, Rybin V, Hassa PO, Uttenweiler A, Reinhardt M, Schmidt A, Seiler J et al (2009) Catalytic core of a membrane-associated eukaryotic polyphosphate polymerase. *Science* 324: 513–516
- Ikeh M, Ahmed Y, Quinn J (2017) Phosphate acquisition and virulence in human fungal pathogens. *Microorganisms* 5: 48
- Ingram SW, Barnes LD (2000) Disruption and overexpression of the *Schizosaccharomyces pombe* aph1 gene and the effects on intracellular diadenosine 5',5'''-P1,P4-tetraphosphate (Ap4A), ATP and ADP concentrations. *Biochem J* 350: 663–669
- Jumper J, Evans R, Pritzel A, Green T, Figurnov M, Ronneberger O, Tunyasuvunakool K, Bates R, Zidek A, Potapenko A et al (2021) Highly accurate protein structure prediction with AlphaFold. *Nature* 596: 583–589
- Klompmaier SH, Kohl K, Fasel N, Mayer A (2017) Magnesium uptake by connecting fluid-phase endocytosis to an intracellular inorganic cation filter. *Nat Commun* 8: 1879
- Lander N, Ulrich PN, Docampo R (2013) Trypanosoma brucei vacuolar transporter chaperone 4 (TbVtc4) is an Acidocalcisome polyphosphate kinase required for in vivo infection. *J Biol Chem* 288: 34205–34216
- Legati A, Giovannini D, Nicolas G, Lopez-Sanchez U, Quintans B, Oliveira JRM, Sears RL, Ramos EM, Spiteri E, Sobrido MJ et al (2015) Mutations in XPR1 cause primary familial brain calcification associated with altered phosphate export. *Nat Genet* 47: 579–581
- Liu J, Yang L, Luan M, Wang Y, Zhang C, Zhang B, Shi J, Zhao FG, Lan W, Luan S (2015) A vacuolar phosphate transporter essential for phosphate homeostasis in *Arabidopsis*. *Proc Natl Acad Sci U S A* 112: E6571–E6578
- Lonetti A, Sziogyarto Z, Bosch D, Loss O, Azevedo C, Saiardi A (2011) Identification of an evolutionarily conserved family of inorganic polyphosphate endopolyphosphatases. *J Biol Chem* 286: 31966–31974
- Mailer RK, Hanel L, Allende M, Renne T (2019) Polyphosphate as a target for interference with inflammation and thrombosis. *Front Med (Lausanne)* 6: 76
- McCarthy L, Abramchuk I, Wafy G, Denoncourt A, Lavallee-Adam M, Downey M (2022) Ddp1 cooperates with Ppx1 to counter a stress response initiated by nonvacuolar polyphosphate. *MBio* 13: e0039022
- Moreno-Sanchez D, Hernandez-Ruiz L, Ruiz FA, Docampo R (2012) Polyphosphate is a novel pro-inflammatory regulator of mast cells and is located in Acidocalcisomes. *J Biol Chem* 287: 28435–28444
- Muller O, Bayer MJ, Peters C, Andersen JS, Mann M, Mayer A (2002) The Vtc proteins in vacuole fusion: coupling NSF activity to V(0) trans-complex formation. *EMBO J* 21: 259–269
- Nair VS, Gu CF, Janoshazi AK, Jessen HJ, Wang HC, Shears SB (2018) Inositol pyrophosphate synthesis by diphosphoinositol pentakisphosphate kinase-1 is regulated by phosphatidylinositol (4,5) bisphosphate. *Biosci Rep* 38: BSR20171549
- Ozalp VC, Nielsen LJ, Olsen LF (2010) An Aptamer-based Nanobiosensor for real-time measurements of ATP dynamics. *ChemBioChem* 11: 2538–2541
- Pavlovic I, Thakor DT, Vargas JR, McKinlay CJ, Hauke S, Anstaett P, Camuña RC, Bigler L, Gasser G, Schultz C (2016) Cellular delivery and

- photochemical release of a caged inositol-pyrophosphate induces PH-domain translocation in cellulose. *Nat Commun* 7: 10622
- Pettersen EF, Goddard TD, Huang CC, Couch GS, Greenblatt DM, Meng EC, Ferrin TE (2004) UCSF chimera?A visualization system for exploratory research and analysis. *J Comput Chem* 25: 1605–1612
- Pluskal T, Hayashi T, Saitoh S, Fujisawa A, Yanagida M (2011) Specific biomarkers for stochastic division patterns and starvation-induced quiescence under limited glucose levels in fission yeast. *FEBS J* 278: 1299–1315
- Puga MI, Mateos I, Charukesi R, Wang Z, Franco-Zorrilla JM, de Lorenzo L, Irigoyen ML, Masiero S, Bustos R, Rodriguez J et al (2014) SPX1 is a phosphate-dependent inhibitor of phosphate starvation response 1 in *Arabidopsis*. *Proc Natl Acad Sci U S A* 111: 14947–14952
- Reese C, Heise F, Mayer A (2005) Trans-SNARE pairing can precede a hemifusion intermediate in intracellular membrane fusion. *Nature* 436: 410–414
- Rohloff P, Docampo R (2008) A contractile vacuole complex is involved in osmoregulation in *Trypanosoma cruzi*. *Exp Parasitol* 118: 17–24
- Schepler H, Neufurth M, Wang SF, She ZD, Schroder HC, Wang XH, Muller WEG (2022) Acceleration of chronic wound healing by bio-inorganic polyphosphate: In vitro studies and first clinical applications. *Theranostics* 12: 18–34
- Sethuraman A, Rao NN, Kornberg A (2001) The endopolyphosphatase gene: essential in *Saccharomyces cerevisiae*. *Proc Natl Acad Sci U S A* 98: 8542–8547
- Smith SA, Morrissey JH (2014) Polyphosphate: a new player in the field of hemostasis. *Curr Opin Hematol* 21: 388–394
- Urech K, Dürr M, Boller T, Wiemken A, Schwencke J (1978) Localization of polyphosphate in vacuoles of *Saccharomyces cerevisiae*. *Arch Microbiol* 116: 275–278
- Uttenweiler A, Schwarz H, Neumann H, Mayer A (2007) The vacuolar transporter chaperone (VTC) complex is required for microautophagy. *Mol Biol Cell* 18: 166–175
- Voglmaier SM, Bembek ME, Kaplin AI, Dormán G, Olszewski JD, Prestwich GD, Snyder SH (1996) Purified inositol hexakisphosphate kinase is an ATP synthase: diphosphoinositol pentakisphosphate as a high-energy phosphate donor. *Proc Natl Acad Sci U S A* 93: 4305–4310
- Wild R, Gerasimaite R, Jung JY, Truffault V, Pavlovic I, Schmidt A, Saiardi A, Jessen HJ, Poirier Y, Hothorn M et al (2016) Control of eukaryotic phosphate homeostasis by inositol polyphosphate sensor domains. *Science* 352: 986–990
- Williams CJ, Headd JJ, Moriarty NW, Prisant MG, Videau LL, Deis LN, Verma V, Keedy DA, Hintze BJ, Chen VB et al (2018) MolProbity: more and better reference data for improved all-atom structure validation. *Protein Sci* 27: 293–315
- Zhang K (2016) Gctf: real-time CTF determination and correction. *J Struct Biol* 193: 1–12
- Zheng SQ, Palovcak E, Armache JP, Verba KA, Cheng Y, Agard DA (2017) MotionCor2: anisotropic correction of beam-induced motion for improved cryo-electron microscopy. *Nat Methods* 14: 331–332
- Zivanov J, Nakane T, Scheres SHW (2020) Estimation of high-order aberrations and anisotropic magnification from cryo-EM data sets in RELION-3.1. *IUCr* 7: 253–267